A CBS-based partitioned semi-implicit coupling algorithm for fluid–structure interaction using MCIBC method

He, Tao

DOI:
10.1016/j.cma.2015.09.020

Document Version
Peer reviewed version

Citation for published version (Harvard):
He, T 2016, 'A CBS-based partitioned semi-implicit coupling algorithm for fluid–structure interaction using MCIBC method', *Computer Methods in Applied Mechanics and Engineering*, vol. 298, pp. 252-278. https://doi.org/10.1016/j.cma.2015.09.020

Accepted Manuscript

A CBS-based partitioned semi-implicit coupling algorithm for fluid–structure interaction using MCIBC method

Tao He

PII: S0045-7825(15)00314-X
DOI: http://dx.doi.org/10.1016/j.cma.2015.09.020
Reference: CMA 10715

To appear in: *Comput. Methods Appl. Mech. Engrg.*

Received date: 9 April 2015
Revised date: 5 August 2015
Accepted date: 25 September 2015

Please cite this article as: T. He, A CBS-based partitioned semi-implicit coupling algorithm for fluid–structure interaction using MCIBC method, *Comput. Methods Appl. Mech. Engrg.* (2015), http://dx.doi.org/10.1016/j.cma.2015.09.020

A CBS-based partitioned semi-implicit coupling algorithm for fluid-structure interaction using MCIBC method

Tao He[a,b,*]

[a]*Department of Civil Engineering, Shanghai Normal University, Shanghai 201418, China*
[b]*School of Civil Engineering, University of Birmingham, Birmingham B15 2TT, UK*

Abstract

The characteristic-based split (CBS) scheme has been extensively utilized to address the fluid sub-problem within fluid-structure interaction (FSI) analyses over the past decade. To cope with FSI, this article develops a CBS-based partitioned semi-implicit coupling algorithm where the CBS scheme serves not only for the fluid component but also for the entire coupling algorithm. At each time instant, the first step of the CBS scheme is explicitly treated together with the fluid mesh movement, while the remaining two steps are implicitly coupled with the structural motion on the fluid mesh frozen temporarily. To retrieve the semi-implicit coupling style, a mass source term is iteratively updated in the pressure Poisson equation for elements adhering to the fluid-structure interface. The present algorithm provides the stabilized solution of the Navier-Stokes equations and the computational reduction without stability drop, thus inheriting the virtues of the CBS scheme and the projection-based semi-implicit coupling method. Within our coupling algorithm, FSI is achieved by the modified combined interface boundary condition (MCIBC) method which is re-derived in a more concise fashion. A weak implementation of the MCIBC method is proposed to avoid deteriorating the numerical results. The MCIBC method rectifies the limitations of its original counterpart, making itself applicable to fluid-rigid/flexible body interaction. Flow-induced vibrations of various bluff bodies are analyzed to test the feasibility of the proposed methodology. The overall numerical results agree well with the existing data, demonstrating the validity and the applicability of the present approach.

Keywords: Fluid-structure interaction, Semi-implicit, CBS, CIBC method

1. Introduction

1.1. Literature review on semi-implicit coupling scheme

As one of challenging topics in computational fluid dynamics, fluid-structure interaction (FSI) has drawn a growing interest from the research community. Partitioned approaches under the arbitrary Lagrangian-Eulerian (ALE) description are in general favored for the numerical solution of such a complicated effect, although monolithic approaches [1, 2] attract some attention. The former approaches are typically classified into explicit coupling algorithms [3, 4] and implicit coupling algorithms [5, 6].

Apart from the above two categories, a third one, known as *semi-implicit* coupling algorithms, have been developed since 2006. Fernández *et al.* [7] first proposed a projection semi-implicit coupling scheme for simulating FSI problems with strong added-mass effect. The basis of this semi-implicit concept depends on the classical Chorin-Témam splitting [8, 9] which naturally offers an explicit-implicit treatment for the FSI resolution. Specially, the ALE-advection-diffusion step (explicit coupling step) is explicitly treated with the predicted fluid mesh while the projection step (implicit coupling step) is implicitly coupled with the structural motion on the previously known fluid mesh. A rigorously theoretical analysis provided in [7] indicated that, when compared to the implicit coupling algorithm, the semi-implicit coupling algorithm exhibts the enhanced computational efficiency without affecting the

*Corresponding author.
Email address: txh317@bham.ac.uk (Tao He)

stability condition significantly. Following the idea of Fernández *et al.* [7], a number of semi-implicit coupling methods have been presented. Quaini and Quarteroni [10] invented a semi-implicit coupling scheme by using the algebraic fractional step method. It is the first time that the algebraic fractional step method is applied to FSI. Different from the differential splitting, the algebraic fractional step method requires no auxiliary boundary conditions for differential subsystems divided by the original problem. Badia *et al.* [11] introduced the inexact block-LU factorization into several semi-implicit coupling schemes and discussed their performances. Astorino *et al.* [12] proposed Nitsche-based and Robin-based semi-implicit coupling schemes, as well as a couple of variants, for an incompressible viscous fluid interplaying with a thin-walled solid. In that paper, the better stability properties were achieved through these hybrid interface conditions. In a simplified FSI system, Astorino *et al.* [13] performed a convergence analysis for the projection-based semi-implicit coupling scheme [7] and proved the error of time discretization to be at least $\sqrt{\Delta t}$ in the scheme. Fernández [14] presented a comprehensive review for the numerical simulations of blood flows in large arteries involving the explicit, semi-implicit and implicit coupling schemes. A new partitioned semi-implicit coupling method was developed on the basis of a general algorithm for fluid dynamics [15–17]. It is seen from [15] that a set of additional ordinary differential equations (ODEs) need to be solved on the constructed fluid-structure interface. Unlike [15], the traditional interface conditions were enforced in [16, 17]. The author's research work was briefly summarized in [16] by comparing different partitioned coupling schemes for two large-displacement FSI problems. Reference [17] provided the details on carrying out the smoothed finite element technique for the structural part of the partitioned solution strategy.

Instead of adopting the Chorin-Témam splitting [8, 9], a handful of partitioned semi-implicit coupling schemes monolithically solve the fluid momentum equation. Sy and Murea [18, 19] solved a least squares problem on the fluid-structure interface so as to ensure the continuity of the velocity and stress in the semi-implicit way. The explicit coupling phase only predicts the fluid mesh while the fluid and solid resolutions are deposited within the implicit iterations. Breuer *et al.* [20] independently designed a partitioned semi-implicit predictor-corrector coupling scheme to study an FSI benchmark case in turbulent flows. Different from [18, 19], the mesh adaptation is repeated at the corrector step (i.e. the implicit coupling step).

1.2. Brief on CBS scheme with applications to moving mesh problems

The *characteristic-based split* (CBS) scheme has been originally proposed by Zienkiewicz *et al.* [21] for fluid dynamics. During the last decade, the CBS scheme has succeeded with respect to the problems involving moving and deformable boundaries. Using the scheme, Nithiarasu [22] numerically simulated the free surface flows within the ALE finite element framework. His work might be the first application of the CBS scheme to the moving mesh problem. After that, many relevant studies have emerged based on different coupling algorithms. For instance, the CBS scheme was employed to settle the forced motion of a circular cylinder with in-line oscillation [23], to compute the viscous free surface on high performance computing systems [24], and to analyze the fluid flow interplaying with a locally flexible airfoil [25]. The noticeable difference between [22] and [23–25] rests with the versions of the CBS scheme, that is to say, the artificially compressible CBS scheme adopted in [22] and the fully incompressible CBS scheme used in [23–25]. For the present, the fully incompressible CBS scheme seems to enjoy more popularity in FSI applications.

The author and his co-workers have conducted a series of FSI studies by using the fully incompressible CBS scheme [15–17, 26–29]. In these studies, the obtained results agree well with available data and some important phenomena of flow-induced vibrations are detected successfully. We implemented the computer simulations on vortex-induced vibrations (VIV) of an oscillating bluff body with different profiles by using the partitioned explicit coupling scheme [26] and the partitioned subiterative coupling schemes [15, 27]. The structural displacment was predicted in [15] while the structural force predictor was employed in [27]. In [15] the effect of dual time steps [30] on FSI was discussed as well. It was found that this stabilization technique would degenerate the numerical results for the aeroelastic problems analyzed therein. Preparatory computations were carried out for the interplay between an elastic solid and incompressible flows [16, 27, 28]. Except [29], a mass source term (MST) [31] was transplanted to the CBS scheme to meet geometric conservation law (GCL) that is difficult to be fulfilled by a fractional-step-type fluid solver. A variant of the CBS scheme [32] was developed to analyze

the more complex vortex dynamics of four oscillating circular cylinders in a square arrangement [29].

From the viewpoint of ALE kinematics, the CBS scheme is also able to cooperate with other spatial discretization techniques. An iterative generalized CBS algorithm in tandem with the adaptive coupled finite element method (FEM) and element-free Galerkin (EFG) method was developed for the non-isothermal non-Newtonian fluid flows in [33]. Zhang *et al.* [34] combined the CBS scheme with the EFG method to cope with free surface flows. Recently, the CBS scheme was introduced into the immersed smoothed FEM for handling the two-dimensional interaction between an incompressible viscous fluid and largely deformable solids [35].

1.3. Motivation of the present study

As reviewed above, a number of moving mesh problems settled by the CBS scheme have shown the computing power of the scheme. Most of these studies however seem tedious since the CBS scheme is just utilized as a fluid subsolver. With this in mind, one primary goal of this paper is to present an innovative use of the CBS scheme. This is inspired by the reality that the CBS scheme complies with the Chorin-Témam splitting [8, 9] which forms the foundation of the projection-based semi-implicit coupling scheme [7]. The proposed method is named the CBS-based partitioned semi-implicit coupling algorithm where the CBS scheme works not only for the fluid subproblem but also for the whole coupling algorithm. The merits of the projection-based semi-implicit coupling method and the CBS scheme are thereby retained in our method. Unlike haemodynamics, the divergence-free condition needs to be properly modified in the projection step of our method for the sake of the genuine semi-implicit style and the enhanced connection amongst subiterations. To the best of the author's knowledge, few efforts are reported on incorporating the CBS scheme with the semi-implicit coupling scheme, except for [15–17] where the limited success was won. The other primary goal of this paper is to reformulate the hybrid interface conditions for FSI computations in order to avoid detours as met before. These conditions are deduced in a straightforward way, hence generating no redundant ODEs on the interface. A weak enforcement of the interface conditions is subsequently proposed to allow for both better quality of the numerical results and fewer computational efforts. This treatment places a special emphasis on the fluid stress tensor and the correction for interfacial displacement. The easier understanding and implementation of these interface conditions are thus acquired. Some other computational details are discussed. In addition, the author is tempted to rectify some errors in his previous papers. The above elements consist of the present work's interests.

The layout of this paper is organized as follows. In Section 2 the governing equations are depicted for the coupled FSI system. The mathematical details of the new hybrid interface conditions are presented in Section 3. Section 4 describes the in-depth procedure of the resulting partitioned semi-implicit coupling algorithm. Several numerical examples are investigated in Section 5 while some conclusions are drawn in the final section.

2. Governing equations

2.1. Fluid problem

The incompressible viscous fluid flows on the moving mesh are dominated by the ALE formulation of the Navier-Stokes (NS) equations as follows

$$\nabla \cdot \mathbf{u} = 0, \tag{1}$$

$$\rho^{\mathrm{F}} \left(\frac{\partial \mathbf{u}}{\partial t} + \mathbf{c} \cdot \nabla \mathbf{u} - \mathbf{f}^{\mathrm{F}} \right) - \nabla \cdot \boldsymbol{\sigma}^{\mathrm{F}} = \mathbf{0}, \tag{2}$$

where ∇ means the gradient operator, $\mathbf{u}$ is the fluid velocity, ρ^{F} is the fluid density, $\mathbf{c} = \mathbf{u} - \mathbf{w}$ is the convective velocity, $\mathbf{w}$ is the mesh velocity, $\mathbf{f}^{\mathrm{F}}$ is the fluid body force, $\boldsymbol{\sigma}^{\mathrm{F}}$ is the fluid stress tensor, and $\mathbf{x}$ and t represent the spatial and temporal coordinates, respectively. The constitutive equation for the Newtonian fluid reads as

$$\boldsymbol{\sigma}^{\mathrm{F}} = -p\mathbf{I} + 2\mu\boldsymbol{\epsilon} \quad \text{and} \quad \boldsymbol{\epsilon} = \frac{1}{2}\left(\nabla\mathbf{u} + (\nabla\mathbf{u})^{\mathrm{T}}\right), \tag{3}$$

where p is the fluid pressure, $\mathbf{I}$ denotes the identity matrix, μ is the fluid viscosity, $\boldsymbol{\epsilon}$ is the rate-of-strain tensor and superscript T indicates transpose. Appropriate boundary and initial conditions should be prescribed to complete the fluid equations.

The following dimensionless scales are defined

$$\mathbf{x}^* = \frac{\mathbf{x}}{D},\ t^* = \frac{tU}{D},\ \mathbf{u}^* = \frac{\mathbf{u}}{U},\ \mathbf{c}^* = \frac{\mathbf{c}}{U},\ p^* = \frac{p}{\rho^{\mathrm{F}}U^2},\ \left(\mathbf{f}^{\mathrm{F}}\right)^* = \frac{\mathbf{f}^{\mathrm{F}}D}{U^2}$$

based on the characteristic velocity U and the characteristic length D. By employing these dimensionless variables and dropping all asterisks, the dimensionless NS equations are obtained as follows

$$\nabla \cdot \mathbf{u} = 0, \tag{4}$$

$$\frac{\partial \mathbf{u}}{\partial t} + \mathbf{c} \cdot \nabla \mathbf{u} - \nabla \cdot \boldsymbol{\sigma}^{\mathrm{F}} - \mathbf{f}^{\mathrm{F}} = \mathbf{0}, \tag{5}$$

with

$$\boldsymbol{\sigma}^{\mathrm{F}} = -p\mathbf{I} + \frac{1}{Re}\left(\nabla \mathbf{u} + (\nabla \mathbf{u})^{\mathrm{T}}\right), \tag{6}$$

where $Re = \rho^{\mathrm{F}}UD/\mu$ is the Reynolds number. Eqs. (4)–(6) are solved by the semi-implicit CBS scheme [21] whose procedure is actualized below

Step 1: Calculate the auxiliary velocity

$$\widetilde{\mathbf{u}} - \mathbf{u}^n = \Delta t \left(-\mathbf{c}^n \cdot \nabla \mathbf{u}^n + \frac{1}{Re}\nabla^2 \mathbf{u}^n + \frac{\Delta t}{2}\mathbf{c}^n \cdot \nabla(\mathbf{c}^n \cdot \nabla \mathbf{u}^n) \right), \tag{7}$$

Step 2: Update the pressure

$$\nabla^2 p^{n+1} = \frac{1}{\Delta t}\nabla \cdot \widetilde{\mathbf{u}}, \tag{8}$$

Step 3: Correct the velocity

$$\mathbf{u}^{n+1} - \widetilde{\mathbf{u}} = -\Delta t \left(\nabla^2 p^{n+1} - \frac{\Delta t}{2}\mathbf{c}^n \cdot \nabla^2 p^n \right), \tag{9}$$

where Δt is the time step, and the body force $\mathbf{f}^{\mathrm{F}}$ and the third-order terms are neglected. Linear three-node triangular (T3) element is used for finite element discretization since the scheme permits the low-order and equal-order interpolation for both velocity and pressure.

2.2. Structural problem

A structure immersed in a fluid sustains the fluctuating fluid force. The structure is thereby modeled as a spring-damper-mass system. The isotropic assumption is made for the structural problem. The structural governing equation is expressed in the Lagrangian description with proper initial and boundary conditions. Newmark-β method [36] is utilized to advance the structural movement in time.

Let us suppose that a rigid body undergoes the translational motion in two dimensions. The structural displacement is represented by $\mathbf{d} = \{d_1,\ d_2\}^{\mathrm{T}}$ where d_1 is the horizontal component and d_2 the vertical component. The mass, damping and stiffness of the structure are denoted by m, c and k. The dimensionless scales

$$\mathbf{x}^* = \frac{\mathbf{x}}{D},\ t^* = \frac{tU}{D},\ \mathbf{d}^* = \frac{\mathbf{d}}{D},\ C_{\mathrm{D}} = \frac{2F_{\mathrm{D}}}{\rho^{\mathrm{F}}U^2D},\ C_{\mathrm{L}} = \frac{2F_{\mathrm{L}}}{\rho^{\mathrm{F}}U^2D},\ m^* = \frac{m}{\rho^{\mathrm{F}}D^2}$$

and the reduced parameters

$$\xi = \frac{c}{2\sqrt{mk}},\ f_{\mathrm{R}} = \frac{f_{\mathrm{N}}D}{U},\ f_{\mathrm{N}} = \frac{1}{2\pi}\sqrt{\frac{k}{m}}$$

are computed for the rigid body, where the drag coefficient C_{D} and the life coefficient C_{L} are the dimensionless force, the mass ratio m^* is the dimensionless mass, F_{D} and F_{L} are the fluid drag and lift, ξ is the damping ratio, f_{R} is the reduced natural frequency, and f_{N} is the natural frequency. By considering the above variables without superscript asterisks, the dimensionless equation of rigid-body motion is written as

$$\ddot{\mathbf{d}} + 4\pi f_{\mathrm{R}}\xi\dot{\mathbf{d}} + (2\pi f_{\mathrm{R}})^2\mathbf{d} = \frac{1}{2m^*}\begin{Bmatrix} C_{\mathrm{D}} \\ C_{\mathrm{L}} \end{Bmatrix}. \tag{10}$$

The law of momentum conservation for a flexible structure reads as

$$\rho^{\mathrm{S}}\left(\ddot{\mathbf{d}} - \mathbf{f}^{\mathrm{S}}\right) - \nabla\cdot\boldsymbol{\sigma}^{\mathrm{S}} = \mathbf{0}, \tag{11}$$

where ρ^{S} is the structural density, $\mathbf{f}^{\mathrm{S}}$ is the structural body force, $\boldsymbol{\sigma}^{\mathrm{S}}$ is the Cauchy stress tensor and the structural damping is omitted. Young's modulus E and Poisson's ratio ν must be prescribed for the solid problem. To accommodate the geometric nonlinearity, the Saint Venant-Kirchhoff constitutive model is specified by

$$\mathbf{S} = \mathbf{C} : \mathbf{E} \quad \text{and} \quad \mathbf{E} = \frac{1}{2}(\mathbf{F}^{\mathrm{T}}\cdot\mathbf{F} - \mathbf{I}), \tag{12}$$

where $\mathbf{S}$ is the second Piola-Kirchhoff stress tensor, $\mathbf{C}$ stands for the constitutive tensor, $\mathbf{E}$ is the Green-Lagrangian strain tensor, and $\mathbf{F} = \mathbf{I} + \nabla\mathbf{d}$ is the deformation gradient tensor. $\mathbf{S}$ is related to $\boldsymbol{\sigma}^{\mathrm{S}}$ via the geometric transformation given by

$$\mathbf{S} = J\mathbf{F}^{-1}\boldsymbol{\sigma}^{\mathrm{S}}\mathbf{F}^{-\mathrm{T}}, \tag{13}$$

where $J = \det(\mathbf{F})$.

Similarly, the following dimensionless scales are defined

$$\mathbf{x}^* = \frac{\mathbf{x}}{D},\ t^* = \frac{tU}{D},\ \mathbf{d}^* = \frac{\mathbf{d}}{D},\ E^* = \frac{E}{\rho^{\mathrm{F}}U^2},\ \left(\mathbf{f}^{\mathrm{S}}\right)^* = \frac{\mathbf{f}^{\mathrm{S}}D}{U^2},\ m^* = \frac{\rho^{\mathrm{S}}}{\rho^{\mathrm{F}}}$$

in order to enable the nondimensionalization of Eq. (11). Discarding all asterisks, the dimensionless equation of flexible-body motion is established as

$$\ddot{\mathbf{d}} - \frac{1}{m^*}\nabla\cdot\boldsymbol{\sigma}^{\mathrm{S}} - \mathbf{f}^{\mathrm{S}} = \mathbf{0}, \tag{14}$$

which is linearized by the Newton-Raphson procedure in total Lagrangian formulation [37]. Besides the traditional FEM, the cell-based smoothed FEM (CS-FEM) [38–40] is used to for the geometrically nonlinear analysis. Interested readers can refer to [28] for more details.

2.3. Mesh deformation method

Our mesh deformation method adopts a blend of moving submesh approach (MSA) [41] and the ortho-semi-torsional spring analogy method [42]. The detailed steps of the method are well illuminated in [26, 28].

To satisfy GCL for unsteady flows on moving mesh, MST [31] is absorbed into the second step of the CBS scheme. Accordingly, Eq. (8) is recast as

$$\nabla^2 p^{n+1} = \frac{1}{\Delta t}\nabla\cdot\tilde{\mathbf{u}} + S_{\mathrm{MST}}^{n+1}, \tag{15}$$

with

$$S_{\mathrm{MST}}^{n+1} = \frac{1}{2A_e^{n+1}}\begin{vmatrix} w_1^2 - w_1^1 & w_2^2 - w_2^1 \\ w_1^3 - w_1^1 & w_2^3 - w_2^1 \end{vmatrix}^{n+1} \quad \text{and} \quad \mathbf{w}^{n+1} = \frac{\mathbf{x}^{n+1} - \mathbf{x}^n}{\Delta t}, \tag{16}$$

where S_{MST} is MST, A_e indicates the area of element e, superscript i (i = 1, 2 and 3) in $\mathbf{w}$ means point i of element e and subscript j (j = 1 and 2) in $\mathbf{w}$ denotes component j of the coordinates. The importance of MST to the semi-implicit coupling will be demonstrated later.

3. Interface coupling conditions

3.1. Traditional interface conditions

Within the partitioned approach, the interplay between a fluid and a structure (or solid) is accomplished on Σ via separately enforcing the velocity continuity

$$\mathbf{u} = \dot{\mathbf{d}}, \tag{17}$$

and the traction equilibrium

$$\mathbf{t}^{\mathrm{F}} = \mathbf{t}^{\mathrm{S}}, \tag{18}$$

where $\mathbf{t}^{\mathrm{F}} = \boldsymbol{\sigma}^{\mathrm{F}} \cdot \mathbf{n}^{\mathrm{S}}$ and $\mathbf{t}^{\mathrm{S}} = \boldsymbol{\sigma}^{\mathrm{S}} \cdot \mathbf{n}^{\mathrm{S}}$ are the fluid and structural tractions respectively, $\mathbf{n}^{\mathrm{S}}$ represents the unit outward normal of Σ pointing from the structure to the fluid and $\mathbf{n}^{\mathrm{S}} = -\mathbf{n}^{\mathrm{F}}$. Also, the following geometric continuity on Σ should be satisfied for the dynamic mesh motion

$$\mathbf{x} = \mathbf{d} \quad \text{and} \quad \mathbf{w} = \dot{\mathbf{d}}. \tag{19}$$

3.2. Reformulation of CIBC method

Based on the pioneering works [43, 44], Jaiman *et al.* [45] has recently proposed new interface coupling conditions to relieve the time lag effect in the partitioned explicit coupling method. This method is termed the *combined interface boundary condition* (CIBC) method that adjusts the interfacial corrections for velocity and traction via a coupling parameter. The CIBC method was verified by a few examples, such as the one-dimensional elastic piston problem [45], the one-dimensional conjugate heat-transfer process [46] and the two-dimensional subsonic flow-shell problem [47]. Some advantages were acknowledged in these examples. In [48], the CIBC method was flexibly equipped with the improved serial staggered procedure [4] and the fluid subcycling [3]. However, the two-dimensional applications are still deficient in the available literature.

The original CIBC method [44, 45] is derived from the convention $\boldsymbol{\sigma}^{\mathrm{F}} = p\mathbf{I}$, making the method run in an awkward way for the NS solvers. Here, the fluid stress takes the form of Eq. (3) to readily re-formulate the CIBC method. The inclusion of the full fluid stress is especially important to low Re flows in which the viscosity plays a significant role.

A unified formulation of the coupled FSI system is written on Σ as

$$\rho^{\mathrm{I}} \dot{\mathbf{u}}^{\mathrm{I}} = \nabla \cdot \boldsymbol{\sigma}^{\mathrm{I}} + \rho^{\mathrm{I}} \mathbf{f}^{\mathrm{I}}, \tag{20}$$

where superscript I = F and S and $\mathbf{u}^{\mathrm{S}} = \dot{\mathbf{d}}$. From the velocity continuity (17), we can obtain the following relation

$$\rho^{\mathrm{F}} \ddot{\mathbf{d}} = \nabla \cdot \boldsymbol{\sigma}^{\mathrm{F}}, \tag{21}$$

where the body force is ignored on Σ. The normal on Σ is not assumed to be time-independent for the infinitesimal deformation.

By differentiating Eq. (18) with respect to t, we derive

$$\dot{\mathbf{t}}^{\mathrm{F}} = \dot{\mathbf{t}}^{\mathrm{S}}. \tag{22}$$

Eqs. (21) and (22) are the foundation of converting the conventional interface conditions into the combined interface conditions. As a result, one new relation for the velocity on the structural side of the interface Σ^{S} is given by

$$\rho^{\mathrm{F}} \ddot{\mathbf{d}} + \omega \dot{\mathbf{t}}^{\mathrm{S}} = \nabla \cdot \boldsymbol{\sigma}^{\mathrm{F}} + \omega \dot{\mathbf{t}}^{\mathrm{F}}, \tag{23}$$

and the other one for the traction on the fluid side of the interface Σ^{F} is written by

$$\omega \dot{\mathbf{t}}^{\mathrm{F}} + \nabla \cdot \boldsymbol{\sigma}^{\mathrm{F}} = \omega \dot{\mathbf{t}}^{\mathrm{S}} + \rho^{\mathrm{F}} \ddot{\mathbf{d}}, \tag{24}$$

where ω is a positive coupling parameter which should be small enough to make sure that the interfacial energy is always stable [44].

In terms of Gauss-Seidel iterations, Eqs. (23) and (24) can be rewritten on two consecutive time levels as

$$\left(\rho^{\mathrm{F}}\ddot{\mathbf{d}}\right)^{n} = \left(\nabla\cdot\boldsymbol{\sigma}^{\mathrm{F}}\right)^{n} - \omega\left(\left(\dot{\mathbf{t}}^{\mathrm{S}}\right)^{n} - \left(\dot{\mathbf{t}}^{\mathrm{F}}\right)^{n}\right), \tag{25}$$

for the velocity on Σ^{S}, and

$$\left(\dot{\mathbf{t}}^{\mathrm{F}}\right)^{n+1} = \left(\dot{\mathbf{t}}^{\mathrm{S}}\right)^{n+1} + \frac{1}{\omega}\left(\left(\rho^{\mathrm{F}}\ddot{\mathbf{d}}\right)^{n+1} - \left(\nabla\cdot\boldsymbol{\sigma}^{\mathrm{F}}\right)^{n+1}\right), \tag{26}$$

for the traction on Σ^{F}. If the fluid density is constant, the corrections for velocity and traction are constructed on two sides of Σ as follows

$$\delta\mathbf{u}^{n} = \frac{\Delta t}{\rho^{\mathrm{F}}}\left(\left(\nabla\cdot\boldsymbol{\sigma}^{\mathrm{F}}\right)^{n} - \omega\left(\left(\dot{\mathbf{t}}^{\mathrm{S}}\right)^{n} - \left(\dot{\mathbf{t}}^{\mathrm{F}}\right)^{n}\right)\right), \tag{27}$$

$$\delta\mathbf{t}^{n+1} = \Delta t\left(\left(\dot{\mathbf{t}}^{\mathrm{S}}\right)^{n+1} + \frac{1}{\omega}\left(\rho^{\mathrm{F}}\ddot{\mathbf{d}}^{n+1} - \left(\nabla\cdot\boldsymbol{\sigma}^{\mathrm{F}}\right)^{n+1}\right)\right), \tag{28}$$

where the coupling parameter ω provides a suitable acceleration-traction joint.

The CIBC method is composed of the corrective increments (27) and (28) that compensate the seperate enforcement of the interface conditions (17) and (18) as follows

$$\mathbf{u}^{n+1} = \dot{\mathbf{d}}^{n+1} + \delta\mathbf{u}^{n}, \tag{29}$$

$$\left(\mathbf{t}^{\mathrm{S}}\right)^{n+1} = \left(\mathbf{t}^{\mathrm{F}}\right)^{n+1} + \delta\mathbf{t}^{n+1}, \tag{30}$$

which are marked as *Correction I*. The fact that the weak imposition of boundary conditions may neglect certain physical processes on the interface, hence introducing the CIBC corrections back into the interfacial conditions increases the physical relevance of the FSI solution [45].

3.3. MCIBC method

As seen above, the new CIBC traction increment also needs the structural traction rate by updating the structural stress field on Σ^{S}. The lack of consistency is thus realized in the interfacial treatment of the structural traction. Specifically, the new structural traction has to be applied to Eq. (28) before it is corrected by Eq. (30). This device poses two major deficiencies: (i) the incapability to deal with fluid-rigid body interaction where no internal stress occurs inside the rigid body and (ii) special procedure may be required for stress prediction in structural dynamics [49]. To circumvent the restricted use of the CIBC method, the modified CIBC (MCIBC) method is proposed in this subsection.

The time derivatives of Eq. (30) at two successive time slices are obtained as

$$\left(\dot{\mathbf{t}}^{\mathrm{S}}\right)^{n} = \left(\dot{\mathbf{t}}^{\mathrm{F}}\right)^{n} + \dot{\delta\mathbf{t}}^{n}, \tag{31}$$

$$\left(\dot{\mathbf{t}}^{\mathrm{S}}\right)^{n+1} = \left(\dot{\mathbf{t}}^{\mathrm{F}}\right)^{n+1} + \dot{\delta\mathbf{t}}^{n+1}. \tag{32}$$

Replacing Eq. (31) into Eq. (27) yields the velocity increment as follow

$$\delta\mathbf{u}^{n} = \frac{\Delta t}{\rho^{\mathrm{F}}}\left(\left(\nabla\cdot\boldsymbol{\sigma}^{\mathrm{F}}\right)^{n} - \omega\dot{\delta\mathbf{t}}^{n}\right). \tag{33}$$

Inserting Eq. (32) into Eq. (26) and considering the style used for Eq. (28), we have the traction increment as follow

$$\delta\mathbf{t}^{n+1} = \frac{\Delta t}{\omega}\left(\left(\nabla\cdot\boldsymbol{\sigma}^{\mathrm{F}}\right)^{n+1} - \rho^{\mathrm{F}}\ddot{\mathbf{d}}^{n+1}\right). \tag{34}$$

Eqs. (33) and (34) constitute the MCIBC formulae where $\dot{\mathbf{t}}^{\mathrm{S}}$ does not appear any more. Both the consistency in the treatment of the interfacial traction and the solvability of fluid-rigid body interaction are recovered in the MCIBC method. Differing from [15, 26], the MCIBC method does not address the first-order ODEs on the interface for traction correction.

The dimensionless MCIBC formulae are expressed as

$$\delta\mathbf{u} = \Delta t \left(\nabla \cdot \boldsymbol{\sigma}^{\mathrm{F}} - \bar{\omega} \dot{\delta\mathbf{t}} \right), \tag{35}$$

$$\delta\mathbf{t} = \frac{\Delta t}{\bar{\omega}} \left(\nabla \cdot \boldsymbol{\sigma}^{\mathrm{F}} - \ddot{\mathbf{d}} \right), \tag{36}$$

where $\bar{\omega}$ is the dimensionless coupling parameter. For the fluid-rigid body interaction, Eqs. (35) and (36) should be integrated along Σ. The underlying nondimensionalization is detailed in the appendix of this paper. Moreover, the displacement continuity on Σ is maintained by

$$\mathbf{x}^{n+1} = \mathbf{d}^{n+1} + \delta\mathbf{u}^{n} \Delta t. \tag{37}$$

3.4. Implementation of MCIBC method

The sequence of subproblems' resolutions seems irrelevant in partitioned FSI computations. Nevertheless, this is not the case with the MCIBC method. Other than *Correction I*, we can adopt

$$\left(\mathbf{t}^{\mathrm{S}}\right)^{n+1} = \left(\mathbf{t}^{\mathrm{F}}\right)^{n+1} + \delta\mathbf{t}^{n}, \tag{38}$$

$$\mathbf{u}^{n+1} = \dot{\mathbf{d}}^{n+1} + \delta\mathbf{u}^{n+1}, \tag{39}$$

with

$$\delta\mathbf{t}^{n} = \frac{\Delta t}{\bar{\omega}} \left(\left(\nabla \cdot \boldsymbol{\sigma}^{\mathrm{F}}\right)^{n} - \ddot{\mathbf{d}}^{n} \right), \tag{40}$$

$$\delta\mathbf{u}^{n+1} = \Delta t \left(\left(\nabla \cdot \boldsymbol{\sigma}^{\mathrm{F}}\right)^{n+1} - \bar{\omega} \dot{\delta\mathbf{t}}^{n} \right). \tag{41}$$

Eqs. (38) and (39) are labeled as *Correction II*. Eq. (40) utilizes $\nabla \cdot \boldsymbol{\sigma}^{\mathrm{F}}$ at time n rather than $n+1$ although the latest fluid variables have already been evaluated. On the other hand, Eq. (41) has to employ $\dot{\delta\mathbf{t}}^{n}$ because $\dot{\delta\mathbf{t}}^{n+1}$ is not obtained yet. Some hysteresis values are therefore used for *Correction II*. In a sense, the difference between *Correction I* and *Correction II* resembles that between the block Jacobi iterations and the block Gauss-Seidel iterations [43].

The numerical tests in [46] show that correcting both interface conditions by the CIBC method may exhibit worse stability properties than correcting either one does. The reasons for this behavior are not clear yet. The present study also confirms that the FSI calculation will deteriorate or even fail when both interface conditions are corrected. To work out this issue, a possible option is to limit the velocity increment, but it is nontrivial to determine the reduction factor. Similar to the displacement predictor-traction corrector scheme [50, 51], a weak treatment of the MCIBC corrections is proposed here. In particular, the velocity increment is used not to correct the structural velocity but to estimate the displacement increment. The traction correction is performed as usual. Regarding the elastic solid, we can further decrease the numerical effort by directly introducing the traction increment into the Galerkin weak formulation of the structural equation to obtain the following equivalent force

$$\overline{\mathbf{F}} = \underbrace{\int_{\Omega^{\mathrm{S}}} \mathbf{N}^{\mathrm{T}} \mathbf{f}^{\mathrm{S}} \mathrm{d}\Omega + \int_{\Gamma_{\mathrm{N}}^{\mathrm{S}}} \mathbf{N}^{\mathrm{T}} \mathbf{h}^{\mathrm{S}} \mathrm{d}\Gamma}_{\widetilde{\mathbf{F}}} + \int_{\Sigma} \mathbf{N}^{\mathrm{T}} \mathbf{t}^{\mathrm{S}} \mathrm{d}\Gamma = \widetilde{\mathbf{F}} + \int_{\Sigma} \mathbf{N}^{\mathrm{T}} \left(\mathbf{t}^{\mathrm{F}} + \delta\mathbf{t} \right) \mathrm{d}\Gamma, \tag{42}$$

where $\mathbf{N}$ is the shape function of the structural element and $\Gamma_{\mathrm{N}}^{\mathrm{S}}$ is the Neumann segment of the structural boundary, and by approximating the velocity increment as

$$\delta\mathbf{u} = \Delta t \nabla \cdot \boldsymbol{\sigma}^{\mathrm{F}}, \tag{43}$$

into which Eq. (35) degenerates if convergent.

As we know, the Courant-Friedrichs-Lewy (CFL) limit has to be held for the explicit numerical scheme because any violation of this condition will engender the unstable or even divergent results. In the CIBC and MCIBC methods, the coupling parameter plays a vital part in the accuracy and stability of the coupled FSI system since it serves as the CFL-like limit by providing the proper velocity-traction coupling on the interface. The coupling parameter may be defined in terms of different notions. In the one-dimensional conjugate heat-transfer process, Roe *et al.* [46] adopted $\theta_{\pm} = \kappa_{\pm}\omega/c_{\pm}\Delta x_{\pm}$ whose optimal value was assessed by the Godunov-Ryabenkii stability analysis. Jaiman *et al.* [45] suggested the approximate scope of $\theta = \omega\|\mathbf{u}\|_{\text{INITIAL}}$ in the one-dimensional piston examples. He *et al.* [15, 26] proposed $\omega' = \omega/\Delta t$ to consider the influence of the time step in VIV simulations. Consequently, the reasonable range of the coupling parameter should be determined for the MCIBC method. It is however too difficult to estimate the optimal value of the coupling parameter in theory, especially for the multi-dimensional cases [45]. We have to utilize the computer experiments to estimate the coupling parameter for each specific problem. In this paper $\bar{\omega} = U\omega$ is defined as the dimensionless coupling parameter. The superior limit of $\bar{\omega}$ is close towards positive infinity, but the inferior limit of $\bar{\omega}$ is not infinitesimal. The former scenario is easily understood from the MCIBC formulae (35) and (36). The explanation for the latter case is simply given as follow. If $\bar{\omega}$ is infinitesimal, then $\delta\mathbf{t}$ will be infinite. The infinite $\delta\mathbf{t}$ violates the fact that the physical information being missed by partitioned computation should be limited, rendering the MCIBC method invalid. In the present study the coupling parameter is chosen according to our previous experience [26].

4. CBS-based partitioned semi-implicit coupling algorithm

Since the CBS scheme obeys the classical Chorin-Témam splitting [8, 9], the CBS-based partitioned semi-implicit coupling scheme is suggested in the fashion similar to [7]. The interface coupling conditions are imposed by the MCIBC method. A second-order structural displacement predictor [3] is introduced into the semi-implicit scheme, entailing the use of *Correction II*. Fixed-point algorithm with Aitken's Δ^2 method [6] is employed to couple the fluid and structural fields owing to its attractive simplicity and efficiency. The procedure of the proposed coupling algorithm is elaborated in the following.

Step 1: Initialize all variables and set $iter = 0$

Step 2: Perform the explicit coupling step

2.1: Extrapolate the position of the interface

$$(\widetilde{\mathbf{x}}_{\Sigma})_{iter}^{n+1} = \mathbf{d}_{\Sigma}^{n} + \left(\frac{3}{2}\dot{\mathbf{d}}_{\Sigma}^{n} - \frac{1}{2}\dot{\mathbf{d}}_{\Sigma}^{n-1}\right)\Delta t$$

2.2: Rearrange the fluid mesh by MSA

2.3: Calculate the mesh velocity

$$\mathbf{w}_{iter}^{n+1} = \frac{\widetilde{\mathbf{x}}_{iter}^{n+1} - \mathbf{x}^{n}}{\Delta t}$$

2.4: Derive the relevant geometric quantities

2.5: Obtain MST for satisfying GCL

$$(S_{\text{MST}})_{iter}^{n+1} = \left(\frac{1}{2A_e}\begin{vmatrix} w_1^2 - w_1^1 & w_2^2 - w_2^1 \\ w_1^3 - w_1^1 & w_2^3 - w_2^1 \end{vmatrix}\right)_{iter}^{n+1}$$

2.6: Compute the intermediate velocity

$$\widetilde{\mathbf{u}} - \mathbf{u}^{n} = \Delta t\left(-\mathbf{c}^{n}\cdot\nabla\mathbf{u}^{n} + \frac{1}{Re}\nabla^2\mathbf{u}^{n} + \frac{\Delta t}{2}\mathbf{c}^{n}\cdot\nabla(\mathbf{c}^{n}\cdot\nabla\mathbf{u}^{n})\right)$$

2.7: Assess the force increment when computing the rigid body

Step 3: Perform the implicit coupling step

3.1: Set $iter \leftarrow iter + 1$

3.2: Update the fluid pressure

$$\nabla^2 p_{iter}^{n+1} = \frac{1}{\Delta t}\nabla \cdot \widetilde{\mathbf{u}} + \left(S_{\mathrm{MST}}\right)_{iter-1}^{n+1}$$

3.3: Correct the fluid velocity

$$\mathbf{u}_{iter}^{n+1} - \widetilde{\mathbf{u}} = -\Delta t\left(\nabla^2 p_{iter}^{n+1} - \frac{\Delta t}{2}\mathbf{c}^n \cdot \nabla^2 p^n\right)$$

3.4: Deduce the fluid load

3.5: Correct the structural force

$$\left(\int_\Sigma \mathbf{t}^{\mathrm{S}}\mathrm{d}\Gamma\right)_{iter}^{n+1} = \left(\int_\Sigma \mathbf{t}^{\mathrm{F}}\mathrm{d}\Gamma\right)_{iter}^{n+1} + \left(\int_\Sigma \delta\mathbf{t}\mathrm{d}\Gamma\right)^n \quad \text{for the rigid body;}$$

$$\overline{\mathbf{F}}_{iter}^{n+1} = \widetilde{\mathbf{F}}_{iter}^{n+1} + \int_\Sigma \left(\left(\mathbf{N}^{\mathrm{T}}\mathbf{t}^{\mathrm{F}}\right)_{iter}^{n+1} + \left(\mathbf{N}^{\mathrm{T}}\right)_{iter}^{n+1}\delta\mathbf{t}^n\right)\mathrm{d}\Gamma \quad \text{for the flexible body}$$

3.6: Solve equation of the structural motion

3.7: Evaluate the velocity increment

$$\delta\mathbf{u}_{iter}^{n+1} = \frac{\Delta t}{S}\int_\Sigma \left(\left(\nabla \cdot \boldsymbol{\sigma}^{\mathrm{F}}\right)_{iter}^{n+1} - \bar{\omega}\dot{\delta\mathbf{t}}^n\right)\mathrm{d}\Gamma \quad \text{for the rigid body;}$$

$$\delta\mathbf{u}_{iter}^{n+1} = \Delta t\left(\nabla \cdot \boldsymbol{\sigma}^{\mathrm{F}}\right)_{iter}^{n+1} \quad \text{for the flexible body}$$

3.8: Maintain the interfacial displacement continuity

$$\left(\mathbf{x}_\Sigma\right)_{iter}^{n+1} = \mathbf{d}_\Sigma^{n+1} + \delta\mathbf{u}_{iter}^{n+1}\Delta t$$

3.9: Estimate the interfacial residuals

$$\mathbf{g}_{iter} = \left|\left(\mathbf{x}_\Sigma\right)_{iter}^{n+1} - \left(\widetilde{\mathbf{x}}_\Sigma\right)_{iter-1}^{n+1}\right|$$

3.10: Check the convergence and the number of iterations:
If not convergent, then go ahead;
Otherwise, proceed to the next time step

3.11: Assess Aitken factor λ_{iter}

3.12: Relax the interface's position

$$\left(\widetilde{\mathbf{x}}_\Sigma\right)_{iter}^{n+1} = \lambda_{iter}\left(\mathbf{x}_\Sigma\right)_{iter}^{n+1} + \left(1 - \lambda_{iter}\right)\left(\widetilde{\mathbf{x}}_\Sigma\right)_{iter-1}^{n+1}$$

3.13: Calculate the new mesh velocity on Σ as the fluid boundary condition

$$\left(\mathbf{w}_\Sigma\right)_{iter}^{n+1} = \frac{\left(\widetilde{\mathbf{x}}_\Sigma\right)_{iter}^{n+1} - \mathbf{x}_\Sigma^n}{\Delta t}$$

3.14: Renew MST for those elements adjacent to the interface

3.15: Return

The pressure Poisson equation will step out of the implicit coupling stage if the approach developed in [7] is immediately applied to the current context. In [15] the pressure is assessed based on the auxiliary velocity and the mesh velocity, both of which are obtained from the explicit coupling stage. The pressure Poisson equation is thereby excluded from the implicit coupling stage. To this end, MST is continuously calculated for those elements sticking to the interface so that the pressure Poisson

equation persists inside the iterative loops. The update of MST is regarded as the enhanced necessity to iterate the field variables per time step and the key to recovery the truly semi-implicit coupling manner.

The projection-based semi-implicit coupling scheme lessens the overall cost without losing the numerical stability [7]. However, this method may not adapt to high Re problems as the pure projection method lacks the stabilized terms which are crucial to suppress spurious pressure oscillations of incompressible NS equations. On the other hand, the CBS scheme is born with stabilizing the fluid solution via its high-order temporal entries in the projection framework. The merits of both methods thus survive in the present coupling algorithm by incorporating one with the other.

The fluid load is computed on the basis of the intermediate velocity in [7]. Instead, we evaluate the fluid force by using the end-of-step velocity. This treatment is consistent with [11]. Another difference between [7] and this paper depends upon the boundary condition for correcting the fluid velocity in the projection step. The predicted mesh velocity is constantly adopted in [7], whereas, seen from Step 3.13, the iterated mesh velocity is employed for the third step of the CBS scheme.

5. Results and discussion

5.1. Numerical examples I: fluid-rigid body interaction

5.1.1. Free oscillations of a circular cylinder

In this example an elastically mounted circular cylinder is allowed to freely oscillate under fully laminar flow conditions. The computational domain and boundary conditions are demonstrated in Fig. 1 where D is the circular cylinder's diameter. The system parameters are set as follows [52]: the reduced natural frequency $f_{\mathrm{R}} = 16.6/Re$, the damping ratio $\xi = 0$, the mass ratio $m^* = 2.5\pi$ and $60 \leqslant Re \leqslant 200$.

For the sake of computational efficiency, the entire computational domain is divided into three parts: the Eulerian subdomain A1, the ALE subdomain A2 and the Lagrangian subdomain A3. The size of A2 is $6D \times 6D$ while that of A3 is $1.2D \times 1.2D$. The grid points in A1 keep fixed at all time while those in A3 move along with the circular cylinder. Only the grid points in A2 are instantaneously updated. To lower the numerical cost further, some time-invariant matrices of elements in A1 are calculated only once at very onset. In Fig. 2(a) the finite element mesh consists of 8092 T3 elements and 4141 points, and the corresponding submesh is demonstrated in Fig. 2(b). The time step is $\Delta t = 1.0 \times 10^{-2}$ and Newmark parameters are $\beta = 0.25$ and $\gamma = 0.5$.

The preliminary study is conducted to assess the effect of the mesh sensitivity and convergence tolerance. The flow past the circular cylinder at $Re = 100$ is considered as the model problem. Three finite element meshes, M1 (8092 T3 elements and 4141 points), M2 (15856 T3 elements and 8033 points) and M3 (31872 T3 elements and 16049 points), are adopted in conjunction with three tolerances, $tol_1 = 1.0 \times 10^{-6}$, $tol_2 = 1.0 \times 10^{-7}$ and $tol_3 = 1.0 \times 10^{-8}$, amounting to nine working cases in total. The computed results are listed in Table 1, including the mean value of horizontal amplitude $d_{1,\mathrm{MEAN}}$ and its root mean square (RMS) $d_{1,\mathrm{RMS}}$, the amplitude of vertical amplitude $d_{2,\mathrm{MAX}}$, the mean value of drag coefficient $C_{\mathrm{D,MEAN}}$ and its RMS $C_{\mathrm{D,RMS}}$, the amplitude of lift coefficient $C_{\mathrm{L,MAX}}$ and the Strouhal number St. In Table 1 an excellent agreement is observed between the computed results and the existing data [15, 26, 52], establishing the validation for further calculations. After examining the obtained data, the difference is quite tiny among the present cases. The cylinder response and aerodynamic parameters are hardly influenced by the mesh resolution and convergence tolerance. M1 and $tol = 1.0 \times 10^{-7}$ are selected for purpose of accuracy and efficiency. Similar tests are not repeated elsewhere for brevity.

Furthermore, it is clearly seen from Table 1 and Fig. 3 that the semi-implicit method is as accurate as the widely-used implicit coupling method but achieves higher efficiency. This trait is valuable for large-scale computations. Although the higher-order treatment on the interface is achieved by the the MCIBC procedure [45], the entire coupling scheme is not the second-order time accurate. The second-order temporal accuracy of the coupling algorithm requires special designs for time integrators of all components of the FSI system [53]. Fig. 4 displays the L_2 norm error in the amplitude when the steady flows are obtained at $Re = 100$. From this figure, the plotted line has a slope of 1.23, clearly

confirming the first-order accuracy of the developed scheme. The same conclusion can be drawn for the second example.

Fig. 5 shows the variation of $d_{2,\mathrm{MAX}}$ and St with Re. Seen from this figure, the lock-in region covers $80 \leqslant Re \leqslant 130$ while that of [52] ranges from $Re = 81$ to $Re = 137$. In Fig. 5(a) $d_{2,\mathrm{MAX}}$ is up to $0.567D$, slightly larger than that of Dejong and Liang [54]. The graph agrees with those of [52] by both increasing and decreasing Re at the lower end of the lock-in region, whereas it is only in accordance with that of [52] by decreasing Re at the upper end. Furthermore, the small rebound is missing at the upper end. In additional to St, St of a rigid cylinder by [26], the Roshko's Re-St relationship [55] and $f_{\mathrm{R}} = 16.6/Re$ are displayed in Fig. 5(b). For the oscillating cylinder, St is dramatically affected by the Re effect and the cylinder oscillations [52]. The flexible cylinder's St obviously departs from the rigid cylinder's within the lock-in region. However, the gap remarkably reduces once Re locates outside the lock-in region. A very small offset is perceived between St and f_{R} during lock-in. These phenomena are interpreted by Prasanth and Mittal [52].

In Fig. 6 vorticity fields are illustrated at two selected Reynolds numbers. The 2S vortex-shedding mode is seen in Fig. 6(a) since the cylinder goes through low-amplitude oscillations at $Re = 75$. Although the cylinder experiences high-amplitude oscillations at $Re = 90$, the C(2S) vortex-shedding mode [56] is not explicitly observed in Fig. 6(b).

The low mass ratio largely accounts for the strong added mass effect in VIV of the bluff body. The impact of mass ratio on the couple fluid-cylinder system [57] was examined by using the MCIBC method in [26]. The mass ratio considered there only reaches $m^* = 1.0$. For the present method, the lowest limit is $m^* \sim 0.5$ under the same conditions.

5.1.2. Free oscillations of a square cylinder

The present problem is concerned with the free oscillations of a square cylinder within a range of Re. The square cylinder with edge length D is placed at zero angle of attack. The problem representation is schematically illustrated in Fig. 7. The physical parameters are defined as [58]: the reduced natural frequency $f_{\mathrm{R}} = 14.39/Re$, the damping ratio $\xi = 0$, the mass ratio $m^* = 10$ and $60 \leqslant Re \leqslant 250$.

The whole domain is broken into the Eulerian subdomain A1 and the ALE subdomain A2. The size of A2 is also $6D \times 6D$. As shown in Fig. 8, the fluid domain is meshed into 16254 T3 elements and 8232 points while a quite coarse submesh is employed for MSA. $\Delta t = 2.0 \times 10^{-2}$, $tol = 1.0 \times 10^{-7}$ and the trapezoidal rule for Newmark-β method are adopted herein.

The obtained data of the $Re = 90$ flow are summarized in Table 2 where $d_{1,\mathrm{MAX}}$ is the peak of horizontal amplitude. Overall, a very good agreement is observed between the obtained and existing data [15, 26, 58]. The data produced by the present semi-implicit coupling method are almost identical to those of [15] and, compared to [26], they are slightly closer to those of [58].

Fig. 9 plots the displacement response and the oscillation frequency f_{O} versus Re. It is apparent that the cylinder's motion is mainly characterized by lock-in and galloping. Galloping is also referred to as *secondary lock-in* in [52]. According to Blevins [59], galloping will be triggered when the bluff body has the non-circular cross-section and the velocity of the incident flow exceeds a certain critical value. Unlike lock-in, galloping drives the vortex-shedding frequency and oscillation amplitude of the bluff body to be several times larger than its natural frequency and the characteristic dimension, respectively. In combination with two panels of this figure, the lock-in region is $87 \leqslant Re \leqslant 100$, forming the first jump of the $d_{2,\mathrm{MAX}}$ curve. Sen and Mittal [58] reported that, for the freely oscillating square cylinder, the width of the lock-in region is roughly a third of the one for the freely oscillating circular cylinder [52]. This fact is confirmed by both this paper and [15]. In Fig. 9(b), galloping is wakened at $Re = 179$ while that of [58] stands at $Re = 175$. The outset of galloping creates the second jump of $d_{2,\mathrm{MAX}}$. In addition to f_{O}, St for the rigid square cylinder [26, 60] and f_{R}, are also plotted in Fig. 9(b). When $100 < Re \leqslant 130$, f_{O} keeps close to St of the stationary cylinder. After the second abrupt decline, the f_{O} curve exhibits a flat fall and gets close to f_{R}. Despite that, the third jump of $d_{2,\mathrm{MAX}}$ takes place at $Re = 220$ in Fig. 9(a). That is to say, galloping is swiftly strengthened if $Re \geqslant 220$. The cylinder displacement will ascend rapidly with the increase of Re during galloping. This behavior can be interpreted by the widely known fact that the galloping instability results from the negative aerodynamic damping [61].

The vortex-shedding modes of the oscillating cylinder at different Re are shown in Fig. 10. The

cylinder response is governed by high-amplitude oscillations at $Re = 87$. It is seen that Fig. 10(a) indicates the 2S mode while [58] reveals the C(2S) mode. The longitudinal spacing between vortices is reduced at $Re = 150$ in Fig. 10(b). The flow pattern is more like the classical 2S mode for the rigid square cylinder. Sen and Mittal [58] reported that the 2P mode [56] would appear for $Re \geqslant 215$. In Fig. 10(c) the vortex-shedding mode at $Re = 230$ resembles its counterpart for the X-Y motion in [58]. Despite that, our previous paper [26] showed a distinct mode that looks like the one for the Y-only motion in [58]. Seen from Fig. 10(d), the vortex sheds at $Re = 250$ in the similar manner.

5.2. Numerical examples II: fluid-flexible body interaction

5.2.1. VIV of a cantilever attached to a square cylinder

This model problem has been originally presented by Wall and Ramm [62] and now becomes the numerical benchmarking to test the capability of FSI solution strategy. The problem settings are schematically demonstrated in Fig. 11. A geometrically nonlinear cantilever is attached to a fixed square cylinder in the center of the downstream face. Due to the unsteady separation of the incompressible viscous flows past the square cylinder, the swirling vortices shed from the cylinder's salient edges with a certain frequency. The vortex formation in the wake of the obstacle generates the time-dependent drag and lift which excite the flexible cantilever to vibrate in the fluid field. The no-slip boundary condition is applied on the surfaces of the cantilever and obstacle. The measuring point is placed in the middle of the right edge of the cantilever. Material parameters of the fluid and solid are specified as [62]: the fluid density $\rho^{\mathrm{F}} = 1.18 \times 10^{-3}$, the fluid viscosity $\mu = 1.82 \times 10^{-4}$, the structural density $\rho^{\mathrm{S}} = 1.0 \times 10^{-1}$, Young's modulus $E = 2.5 \times 10^{6}$ and Poisson's ratio $\nu = 0.35$. The length scale of the square cylinder is $D = 1$ and the inflow velocity is $U = 51.3$, corresponding to $Re = 332.6$ in this example.

The fluid field is decomposed into the Eulerian subdomain A1 and the ALE subdomain A2. A2 is a square box of size $6D \times 6D$. T3 elements are used for the fluid mesh and MSA submesh. The flexible cantilever is discretized with nine-node quadrilateral (Q9) plane stress elements for FEM, and four-node quadrilateral (Q4) plane stress elements for CS-FEM. The meshing information is summarized in Table 3. Fig. 12 exhibits the fluid mesh and MSA submesh for Case 1. In Fig. 13 a Q4 element is typically subdivided into four exactly equivalent rectangular smoothing domains (SDs), relying on the stability condition of CS-FEM [38, 39]. Of total nine points, extra five points are generated to compute the so-called smoothed shape functions by simply averaging the values at four corners. The time step is set as $\Delta t = 1.0 \times 10^{-2}$ and the tolerance is $tol = 1.0 \times 10^{-6}$. Newmark parameters $\beta = 0.5$ and $\gamma = 0.8$ are chosen to eliminate the high-frequency noise in the structural vibrations.

Two key parameters are calculated to assess the performance of the present CBS-based partitioned semi-implicit coupling algorithm. Table 4 lists the time-averaged vertical deflection $d_{2,\mathrm{MEAN}}$ and the time-averaged oscillation frequency $f_{\mathrm{O,MEAN}}$ of the measuring point, as well as those data documented in the open literature [5, 62–72]. The data of Case 1 are identical with most of available ones. In Case 2 $d_{2,\mathrm{MEAN}} = 0.92$ is acceptable, compared with the values in [63, 71, 72]. $f_{\mathrm{O,MEAN}} = 0.0586$ in Case 1 and $f_{\mathrm{O,MEAN}} = 0.0622$ in Case 2 are very close to the first eigenfrequency of the cantilever $f_1^{\mathrm{S}} = 0.0591$ that predominates the structural oscillations. Based on the above analysis, a good agreement is observed from Table 4.

Likewise, Table 4 and Fig. 14 suggest that the semi-implicit method shows the good accuracy and the improved efficiency, especially for the stringent convergence tolerance. Fig. 15 examines the standard L_2 norm error in the tip deflection of the measuring point. Again, the proposed algorithm is proved to be the first-order time accurate since the slope of the line displayed in that picture is 1.173. The identical results are generated in the restrictor flap problem.

Fig. 16 plots the smooth and undamped time histories of tip displacement for both cases, where the unsteady periodic long-term oscillatory movements of the geometrically nonlinear solid are produced correctly. In accordance with [5, 67], the violent strcutural vibrations commences roughly at dimensionless time 100 or at real time of $2s$. Nevertheless, the unsteady long-periodic response of the cantilever was established much later in [66]. Observed from Fig. 16, the amplitude of tip displacement in Case 2 is smaller than that in Case 1, and the slightly longer time is required to reach the characteristic amplitude in this case. Perhaps, the number of Q4 elements and linear shape function

are responsible for the underestimated tip deflection. It should be noticed that the amplitudes are still small in [71, 72] even if much denser finite volume cells are adopted for the cantilever.

According to [66], the displacement history is partitioned into two stages: lock-in and beating. The structural displacement is gradually amplified within the first stage. Meanwhile, the cantilever's oscillation frequency gets close to its first eigenfrequency, inspiring the so-called lock-in or resonance. At the second stage, the structural response converges to the stable long-term oscillatory motion, forming the beating or modulation phenomenon. During the whole course, vortex shedding induces lock-in and drives the cantilever to oscillate sharply. Correspondingly, the violent oscillations of the flexible cantilever significantly alter the vortex-shedding mode whose frequency deviates from the cantilever's first eigenfrequency.

When the stable structural oscillations are fully built up, three typical snapshots of vorticity and pressure fields are graphically displayed in Fig. 17. It is seen that the unsteady features of flow patterns and structural oscillations are evidently distinguished in different phases during an oscillation period. In Fig. 17(a), vortices act on the cantilever surface while being alternatively shed from two lateral sides of the square cylinder. The strong structural oscillations are therefore motivated. Note that the vortices on one side towards which the flexible cantilever starts to move are weakened and are eventually suppressed by the flows near the cantilever. High compression is perceived on this side as well. However, vortices on the opposite side are strengthened and advect downstream from the cantilever. These vortices are generated by velocity gradient at the tip of the flapping cantilever [72]. In Fig. 17(b) the pressure distribution on the frontal side of the square cylinder is positive because of the immediate exposure of the obstacle to the flows, but high suction (the blue zone) is detected along the lateral sides of the square cylinder. The pressure distribution on the cantilever surface opposite to the direction of the structural motion is negative but results in the lower suction.

5.2.2. A restrictor flap in a uniform channel flow

The last example is a flexible restrictor flap in a uniform channel flow [71]. The problem definition is sketched in Fig. 18. The measuring point is put at the flap's upper left corner. Systematic properties are set as follows [71]: the fluid density $\rho^{\mathrm{F}} = 1.0$, the fluid viscosity $\mu = 1.0 \times 10^{-3}$, the structural density $\rho^{\mathrm{S}} = 1000$ for Case A and $\rho^{\mathrm{S}} = 62.5$ for Case B, Young's modulus $E = 6.0 \times 10^4$ and Poisson's ratio $\nu = 0.45$, the inflow velocity $U = 1$, the flap's height $D = 1$ and the Reynolds number is $Re = 1000$.

The fluid domain is divided into the Eulerian subdomain A1 and the ALE subdomain A2. Given the feature of the structural motion, the proportion of A2 is designated as $2.5D \times 1.5D$. For FEM, Eight-node quadrilateral (Q8) plane stress element is utilized to discretize the restrictor flap. The mesh information is listed in Table 5. The fluid mesh and MSA submesh for Case 1 are exposed in Fig. 19. The time step $\Delta t = 5.0 \times 10^{-3}$, the tolerance $tol = 1.0 \times 10^{-6}$ and Newmark parameters $\beta = 0.5$ and $\gamma = 0.8$ are employed here.

The time evolutions of horizontal displacements among various cases are depicted in Fig. 20. Consistent with [71], the obtained magnitudes of tip deflection are approximately 0.6 in both FEM and CS-FEM. Case 1 and Case 2 produce the almost identical amplitudes for two structural densities. This may be caused by the small Young's modulus. Based on the further observation of Fig. 20, the computed results of Case A agree better with that of [71], whereas the curves of Case B diverge from that of [71] very soon. For Case A, the decaying oscillations are observed between [71] and this paper. This phenomenon is explained as follows: when the structural density is large, the vibrations of the restrictor flap are mainly excited by the structural inertia and the fluid serves as the damped oscillator. The decay of tip oscillations in Case B is fairly rapid in this study, although the structural oscillations sustained by the tip vortex shedding remain significant in [71]. When the structural density decreases, our restrictor flap's motion is damped sharply by the fluid action and soon its vibrations trend to be feeble. This behavior has been seen in an analogous example [73] where the structural movement becomes nearly stationary over an expanded period of time. The typical contours of the horizontal fluid velocity at different time slices are displayed in Fig. 21 for Case A.

6. Conclusions

To numerically simulate the transient FSI problems, this paper has presented an efficient partitioned semi-implicit coupling strategy by using a dimensionless ALE finite element formulation. The developed method has been applied to various FSI problems. The obtained results agree with well-documented data and some well-known flow phenomena are detected successfully. The main contributions are summarized as follows:

1. A CBS-based partitioned semi-implicit coupling algorithm is developed. To recover the real semi-implicit style, MST embedded in the second step of the CBS scheme is iteratively computed for those elements next to the interface. The algorithm inherits the improved efficiency from its projection-based counterpart and the stabilized solution from the CBS scheme.
2. The MCIBC method is developed to account for FSI in the semi-implicit coupling algorithm, remedying the drawbacks of the CIBC method.
   (a) The CIBC method is re-deduced in accordance with the complete form of the fluid stress tensor.
   (b) The simpler derivation of the MCIBC method is recognized since no ODEs yield on the interface for the traction increment.
   (c) A weak implementation of the MCIBC method is proposed to be free from the worsened numerical results. The displacement rather than the velocity is corrected on the interface. For the elastic solid, the traction correction term is imported into the Galerkin weak formulation, hence alleviating the programming effort.
3. Other computational aspects are considered. For instance, CS-FEM is utilized to solve the flexible structure for comparison. The dimensionless MCIBC formulae are provided. The correction order of the MCIBC method is discussed.

Although some new developments have been reported in this presentation, more investment is demanded to promote the numerical method.

Acknowledgement

Supports from Innovation Program of Shanghai Municipal Education Commission (grant No.: 14ZZ129), Natural Science Foundation of Shanghai (grant No.: 13ZR1430500) and Capacity Building Program for Local Universities of Shanghai Municipal Science and Technology Commission (grant No.: 14200503000) are gratefully acknowledged. The author wishes to thank anonymous referees for their helpful comments in improving this paper.

Appendix A.

Appendix A.1. Dimensionless MCIBC formulation for rigid-body dynamics

In the equation governing the rigid-body motion, the external load is nondimensionalized as follow

$$\begin{aligned}\frac{D}{mU^2}\begin{Bmatrix}F_1\\F_2\end{Bmatrix} &= \frac{D}{mU^2}\begin{Bmatrix}F_{\mathrm{D}}\\F_{\mathrm{L}}\end{Bmatrix} + \frac{D}{mU^2}\begin{Bmatrix}\delta b_1\\\delta b_2\end{Bmatrix}\\ &= \frac{D}{mU^2}\cdot\frac{1}{2}\rho^{\mathrm{F}}U^2D\begin{Bmatrix}C_{\mathrm{D}}\\C_{\mathrm{L}}\end{Bmatrix} + \frac{D}{mU^2}\cdot\rho^{\mathrm{F}}U^2D\begin{Bmatrix}\delta b_1^*\\\delta b_2^*\end{Bmatrix}\\ &= \frac{1}{2m^*}\begin{Bmatrix}C_{\mathrm{D}}\\C_{\mathrm{L}}\end{Bmatrix} + \frac{1}{m^*}\begin{Bmatrix}\delta b_1^*\\\delta b_2^*\end{Bmatrix},\end{aligned} \tag{A1}$$

where $\{F_1,\ F_2\}^{\mathrm{T}}$ is the external load already corrected by the MCIBC method and $\delta\mathbf{b} = \{\delta b_1,\ \delta b_2\}^{\mathrm{T}}$ is the traction increment.

Introducing the following dimensionless scales

$$\mathbf{x}^* = \frac{\mathbf{x}}{D},\ t^* = \frac{tU}{D},\ \mathbf{u}^* = \frac{\mathbf{u}}{U},\ \mathbf{d}^* = \frac{\mathbf{d}}{D},\ p^* = \frac{p}{\rho^{\mathrm{F}}U^2},\ \Gamma^* = \frac{\Gamma}{D}$$

into Eq. (34) without temporal discretization, we have

$$\begin{aligned}\delta\mathbf{b} &= \int_\Sigma \delta\mathbf{t}\mathrm{d}\Gamma = \frac{\Delta t}{\omega}\int_\Sigma \left(\nabla\cdot\boldsymbol{\sigma}^{\mathrm{F}} - \rho^{\mathrm{F}}\ddot{\mathbf{d}}\right)\mathrm{d}\Gamma \\ &= \rho^{\mathrm{F}}UD\cdot\frac{\Delta t^*}{\omega}\int_\Sigma \left(\left(\nabla\cdot\boldsymbol{\sigma}^{\mathrm{F}}\right)^* - \ddot{\mathbf{d}}^*\right)\mathrm{d}\Gamma^* \\ &= \rho^{\mathrm{F}}U^2D\cdot\frac{\Delta t^*}{U\omega}\int_\Sigma \left(\left(\nabla\cdot\boldsymbol{\sigma}^{\mathrm{F}}\right)^* - \ddot{\mathbf{d}}^*\right)\mathrm{d}\Gamma^*.\end{aligned} \tag{A2}$$

If we define $\bar{\omega} = U\omega$ and drop all asterisks, then Eq. (A2) is nondimensionalized as

$$\delta\mathbf{b} = \frac{\Delta t}{\bar{\omega}}\int_\Sigma \left(\nabla\cdot\boldsymbol{\sigma}^{\mathrm{F}} - \ddot{\mathbf{d}}\right)\mathrm{d}\Gamma = \frac{\Delta t}{\bar{\omega}}\left(\int_\Sigma \nabla\cdot\boldsymbol{\sigma}^{\mathrm{F}}\mathrm{d}\Gamma - S\ddot{\mathbf{d}}\right), \tag{A3}$$

where $S = \int_\Sigma \mathrm{d}\Gamma$.

Substituting the afore-mentioned dimensionless scales into Eq. (33) without temporal discretization, we have

$$\delta\mathbf{u} = \frac{\Delta t}{\rho^{\mathrm{F}}S}\int_\Sigma \left(\nabla\cdot\boldsymbol{\sigma}^{\mathrm{F}} - \omega\dot{\delta\mathbf{t}}\right)\mathrm{d}\Gamma = U\cdot\frac{\Delta t^*}{S^*}\int_\Sigma \left(\left(\nabla\cdot\boldsymbol{\sigma}^{\mathrm{F}}\right)^* - U\omega\dot{\delta\mathbf{t}}^*\right)\mathrm{d}\Gamma^*. \tag{A4}$$

Since the velocity continuity is nondimensionalized by U on the interface, Eq. (A4) is simplified as

$$\delta\mathbf{u} = \frac{\Delta t}{S}\int_\Sigma \left(\nabla\cdot\boldsymbol{\sigma}^{\mathrm{F}} - \bar{\omega}\dot{\delta\mathbf{t}}\right)\mathrm{d}\Gamma = \frac{\Delta t}{S}\int_\Sigma \nabla\cdot\boldsymbol{\sigma}^{\mathrm{F}}\mathrm{d}\Gamma - \frac{\Delta t\bar{\omega}}{S}\dot{\delta\mathbf{b}}. \tag{A5}$$

Appendix A.2. Dimensionless MCIBC formulation for flexible-body dynamics

For the flexible-body equation, the external load is nondimensionalized by

$$E^* = \frac{E}{\rho^{\mathrm{F}}U^2} \quad \text{or} \quad \left(\boldsymbol{\sigma}^{\mathrm{S}}\right)^* = \frac{\boldsymbol{\sigma}^{\mathrm{S}}}{\rho^{\mathrm{F}}U^2}. \tag{A6}$$

By adopting the afore-defined dimensionless scales, the traction increment is expressed as

$$\begin{aligned}\delta\mathbf{t} &= \frac{\Delta t}{\omega}\left(\nabla\cdot\boldsymbol{\sigma}^{\mathrm{F}} - \rho^{\mathrm{F}}\ddot{\mathbf{d}}\right) = \rho^{\mathrm{F}}U\cdot\frac{\Delta t^*}{\omega}\left(\left(\nabla\cdot\boldsymbol{\sigma}^{\mathrm{F}}\right)^* - \ddot{\mathbf{d}}^*\right) \\ &= \rho^{\mathrm{F}}U^2\cdot\frac{\Delta t^*}{U\omega}\left(\left(\nabla\cdot\boldsymbol{\sigma}^{\mathrm{F}}\right)^* - \ddot{\mathbf{d}}^*\right),\end{aligned} \tag{A7}$$

which amounts to

$$\delta\mathbf{t} = \frac{\Delta t}{\bar{\omega}}\left(\nabla\cdot\boldsymbol{\sigma}^{\mathrm{F}} - \ddot{\mathbf{d}}\right). \tag{A8}$$

The velocity increment is obtained by

$$\delta\mathbf{u} = \frac{\Delta t}{\rho^{\mathrm{F}}}\left(\nabla\cdot\boldsymbol{\sigma}^{\mathrm{F}} - \omega\dot{\delta\mathbf{t}}\right) = U\cdot\Delta t^*\left(\left(\nabla\cdot\boldsymbol{\sigma}^{\mathrm{F}}\right)^* - U\omega\dot{\delta\mathbf{t}}^*\right), \tag{A9}$$

which is nondimensionalized as

$$\delta\mathbf{u} = \Delta t\left(\nabla\cdot\boldsymbol{\sigma}^{\mathrm{F}} - \bar{\omega}\dot{\delta\mathbf{t}}\right). \tag{A10}$$

References

[1] J. Liu, R. K. Jaiman, P. S. Gurugubelli, A stable second-order scheme for fluid-structure interaction with strong added-mass effects, Journal of Computational Physics 270 (2014) 687–710.

[2] R. K. Jaiman, S. Sen, P. S. Gurugubelli, A fully implicit combined field scheme for freely vibrating square cylinders with sharp and rounded corners, Computers & Fluids 112 (2015) 1–18.

[3] S. Piperno, Explicit/implicit fluid/structure staggered procedures with a structural predictor and fluid subcycling for 2D inviscid aeroelastic simulations, International Journal for Numerical Methods in Fluids 25 (10) (1997) 1207–1226.

[4] C. Farhat, M. Lesoinne, Two efficient staggered algorithms for the serial and parallel solution of three-dimensional nonlinear transient aeroelastic problems, Computer Methods in Applied Mechanics and Engineering 182 (3) (2000) 499–515.

[5] W. Dettmer, D. Perić, A computational framework for fluid-structure interaction: Finite element formulation and applications, Computer Methods in Applied Mechanics and Engineering 195 (41-43) (2006) 5754–5779.

[6] U. Küttler, W. A. Wall, Fixed-point fluid-structure interaction solvers with dynamic relaxation, Computational Mechanics 43 (1) (2008) 61–72.

[7] M. A. Fernández, J.-F. Gerbeau, C. Grandmont, A projection semi-implicit scheme for the coupling of an elastic structure with an incompressible fluid, International Journal for Numerical Methods in Engineering 69 (4) (2007) 794–821.

[8] A. J. Chorin, Numerical solution of the Navier-Stokes equations, Mathematics of Computation 22 (104) (1968) 745–762.

[9] R. Témam, Une méthode d'approximation de la solution des équations de Navier-Stokes, Bulletin de la Société Mathématique de France 96 (1968) 115–152.

[10] A. Quaini, A. Quarteroni, A semi-implicit approach for fluid-structure interaction based on an algebraic fractional step method, Mathematical Models and Methods in Applied Sciences 17 (6) (2007) 957–983.

[11] S. Badia, A. Quaini, A. Quarteroni, Splitting methods based on algebraic factorization for fluid-structure interaction, SIAM Journal on Scientific Computing 30 (4) (2008) 1778–1805.

[12] M. Astorino, F. Chouly, M. A. Fernández, Robin based semi-implicit coupling in fluid-structure interaction: stability analysis and numerics, SIAM Journal on Scientific Computing 31 (6) (2009) 4041–4065.

[13] M. Astorino, C. Grandmont, Convergence analysis of a projection semi-implicit coupling scheme for fluid-structure interaction problems, Numerische Mathematik 116 (4) (2010) 721–767.

[14] M. A. Fernández, Coupling schemes for incompressible fluid-structure interaction: implicit, semi-implicit and explicit, SeMa Journal 55 (1) (2011) 59–108.

[15] T. He, D. Zhou, Z. Han, J. Tu, J. Ma, Partitioned subiterative coupling schemes for aeroelasticity using combined interface boundary condition method, International Journal of Computational Fluid Dynamics 28 (6-10) (2014) 272–300.

[16] T. He, Partitioned coupling strategies for fluid-structure interaction with large displacement: Explicit, implicit and semi-implicit schemes, Wind & Structures 20 (3) (2015) 423–448.

[17] T. He, Semi-implicit coupling of CS-FEM and FEM for the interaction between a geometrically nonlinear solid and an incompressible fluid, International Journal of Computational Methods 12 (5) (2015) 1550025.

[18] S. Sy, C. M. Murea, A stable time advancing scheme for solving fluid-structure interaction problem at small structural displacements, Computer Methods in Applied Mechanics and Engineering 198 (2) (2008) 210–222.

[19] C. M. Murea, S. Sy, A fast method for solving fluid-structure interaction problems numerically, International Journal for Numerical Methods in Fluids 60 (10) (2009) 1149–1172.

[20] M. Breuer, G. De Nayer, M. Münsch, T. Gallinger, R. Wüchner, Fluid-structure interaction using a partitioned semi-implicit predictor-corrector coupling scheme for the application of large-eddy simulation, Journal of Fluids and Structures 29 (2012) 107–130.

[21] O. C. Zienkiewicz, P. Nithiarasu, R. Codina, M. Vazquez, P. Ortiz, The characteristic-based-split procedure: An efficient and accurate algorithm for fluid problems, International Journal for Numerical Methods in Fluids 31 (1) (1999) 359–392.

[22] P. Nithiarasu, An arbitrary Lagrangian Eulerian (ALE) formulation for free surface flows using the characteristic-based split (CBS) scheme, International Journal for Numerical Methods in Fluids 48 (12) (2005) 1415–1428.

[23] M. R. H. Nobari, H. Naderan, A numerical study of flow past a cylinder with cross flow and inline oscillation, Computers & Fluids 35 (4) (2006) 393–415.

[24] C. A. Klettner, I. Eames, Viscous free surface simulations with the characteristic based split scheme, Computers & Fluids 71 (2013) 487–495.

[25] W. Kang, J. Zhang, P. Lei, M. Xu, Computation of unsteady viscous flow around a locally flexible airfoil at low Reynolds number, Journal of Fluids and Structures 46 (2014) 42–58.

[26] T. He, D. Zhou, Y. Bao, Combined interface boundary condition method for fluid-rigid body interaction, Computer Methods in Applied Mechanics and Engineering 223 (2012) 81–102.

[27] T. He, A partitioned implicit coupling strategy for incompressible flow past an oscillating cylinder, International Journal of Computational Methods 12 (2) (2015) 1550012.

[28] T. He, On a partitioned strong coupling algorithm for modeling fluid-structure interaction, International Journal of Applied Mechanics 7 (2) (2015) 1550021.

[29] Z. Han, D. Zhou, T. He, J. Tu, C. Li, K. C. S. Kwok, C. Fang, Flow-induced vibrations of four circular cylinders with square arrangement at low Reynolds numbers, Ocean Engineering 96 (2015) 21–33.

[30] P. Nithiarasu, O. C. Zienkiewicz, On stabilization of the CBS algorithm: Internal and external time steps, International Journal for Numerical Methods in Engineering 48 (6) (2000) 875–880.

[31] Y.-J. Jan, T. W.-H. Sheu, Finite element analysis of vortex shedding oscillations from cylinders in the straight channel, Computational Mechanics 33 (2) (2004) 81–94.

[32] Z. Han, D. Zhou, J. Tu, C. Fang, T. He, Flow over two side-by-side square cylinders by CBS finite element scheme of Spalart-Allmaras model, Ocean Engineering 87 (2014) 40–49.

[33] Q. Duan, X. Li, An ALE based iterative CBS algorithm for non-isothermal non-Newtonian flow with adaptive coupled finite element and meshfree method, Computer Methods in Applied Mechanics and Engineering 196 (49) (2007) 4911–4933.

[34] X. H. Zhang, J. Ouyang, L. Zhang, The characteristic-based split (CBS) meshfree method for free surface flow problems in ALE formulation, International Journal for Numerical Methods in Fluids 65 (7) (2011) 798–811.

[35] Z.-Q. Zhang, G. R. Liu, B. C. Khoo, Immersed smoothed finite element method for two dimensional fluid-structure interaction problems, International Journal for Numerical Methods in Engineering 90 (10) (2012) 1292–1320.

[36] N. M. Newmark, A method of computation for structural dynamics, Journal of Engineering Mechanics-ASCE 85 (3) (1959) 67–94.

[37] K.-J. Bathe, E. Ramm, E. L. Wilson, Finite element formulations for large deformation dynamic analysis, International Journal for Numerical Methods in Engineering 9 (2) (1975) 353–386.

[38] G. R. Liu, K. Y. Dai, T. T. Nguyen, A smoothed finite element method for mechanics problems, Computational Mechanics 39 (6) (2007) 859–877.

[39] K. Y. Dai, G. R. Liu, Free and forced vibration analysis using the smoothed finite element method (SFEM), Journal of Sound and Vibration 301 (3) (2007) 803–820.

[40] X. Y. Cui, G. R. Liu, G. Y. Li, X. Zhao, T. T. Nguyen, G. Y. Sun, A smoothed finite element method (SFEM) for linear and geometrically nonlinear analysis of plates and shells, CMES: Computer Modeling in Engineering & Sciences 28 (2) (2008) 109–126.

[41] E. Lefrançois, A simple mesh deformation technique for fluid-structure interaction based on a submesh approach, International Journal for Numerical Methods in Engineering 75 (9) (2008) 1085–1101.

[42] G. A. Markou, Z. S. Mouroutis, D. C. Charmpis, M. Papadrakakis, The ortho-semi-torsional (OST) spring analogy method for 3D mesh moving boundary problems, Computer Methods in Applied Mechanics and Engineering 196 (4) (2007) 747–765.

[43] X. Feng, Analysis of finite element methods and domain decomposition algorithms for a fluid-solid interaction problem, SIAM Journal on Numerical Analysis 38 (4) (2001) 1312–1336.

[44] R. K. Jaiman, X. Jiao, P. H. Geubelle, E. Loth, Conservative load transfer along curved fluid-solid interface with non-matching meshes, Journal of Computational Physics 218 (1) (2006) 372–397.

[45] R. Jaiman, P. Geubelle, E. Loth, X. Jiao, Combined interface boundary condition method for unsteady fluid-structure interaction, Computer Methods in Applied Mechanics and Engineering 200 (1) (2011) 27–39.

[46] B. Roe, R. Jaiman, A. Haselbacher, P. H. Geubelle, Combined interface boundary condition method for coupled thermal simulations, International Journal for Numerical Methods in Fluids 57 (3) (2008) 329–354.

[47] R. Jaiman, P. Geubelle, E. Loth, X. Jiao, Transient fluid-structure interaction with non-matching spatial and temporal discretizations, Computers & Fluids 50 (1) (2011) 120–135.

[48] R. Jaiman, P. Geubelle, E. Loth, X. Jiao, Stable and accurate loosely-coupled scheme for unsteady fluid-structure interaction, in: *In* Proceedings of the 45th AIAA Aerospace Sciences Meeting and Exhibit, American Institute of Aeronautics and Astronautics, Reno, Nevada, USA, 2007, pp. 1–28.

[49] D. J. Payen, K.-J. Bathe, A stress improvement procedure, Computers & Structures 112-113 (2012) 311–326.

[50] R. K. Jaiman, Advances in ALE based fluid-structure interaction modeling for offshore engineering applications, in: J. Eberhardsteiner, H. Böhm, F. Rammerstorfer (Eds.), *In* Proceedings of the 6th European Congress on Computational Methods in Applied Sciences and Engineering (ECCOMAS 2012), Vienna, Austria, 2012, pp. 1–11.

[51] R. K. Jaiman, F. Shakib, O. H. Oakley, Y. Constantinides, Fully coupled fluid-structure interaction for offshore applications, in: *In* Proceedings of the 28th International Conference on Ocean, Offshore and Arctic Engineering, American Society of Mechanical Engineers, Honolulu, Hawaii, USA, 2009, pp. 757–765.

[52] T. K. Prasanth, S. Mittal, Vortex-induced vibrations of a circular cylinder at low Reynolds numbers, Journal of Fluid Mechanics 594 (2008) 463–491.

[53] C. Farhat, K. G. van der Zee, P. Geuzaine, Provably second-order time-accurate loosely-coupled solution algorithms for transient nonlinear computational aeroelasticity, Computer Methods in Applied Mechanics and Engineering 195 (17-18) (2006) 1973–2001.

[54] A. DeJong, C. Liang, Parallel spectral difference method for predicting 3D vortex-induced vibrations, Computers & Fluids 98 (2014) 17–26.

[55] A. Roshko, On the development of turbulent wakes from vortex streets, Tech. Rep. NACA TN 1191, National Advisory Committee for Aeronautics (1954).

[56] C. H. K. Williamson, A. Roshko, Vortex formation in the wake of an oscillating cylinder, Journal of Fluids and Structures 2 (4) (1988) 355–381.

[57] C. Y. Zhou, R. M. C. So, K. Lam, Vortex-induced vibrations of an elastic circular cylinder, Journal of Fluids and Structures 13 (2) (1999) 165–189.

[58] S. Sen, S. Mittal, Free vibration of a square cylinder at low Reynolds numbers, Journal of Fluids and Structures 27 (5) (2011) 875–884.

[59] R. D. Blevins, Flow-Induced Vibration, Van Nostrand Reinhold Co. Inc., New York, USA, 1990.

[60] S. Sen, S. Mittal, G. Biswas, Flow past a square cylinder at low Reynolds numbers, International Journal for Numerical Methods in Fluids 67 (9) (2011) 1160–1174.

[61] G. V. Parkinson, J. D. Smith, The square prism as an aeroelastic non-linear oscillator, The Quarterly Journal of Mechanics and Applied Mathematics 17 (2) (1964) 225–239.

[62] E. Ramm, W. Wall, Fluid-structure interaction based upon a stabilized (ALE) finite element method, in: S. Idelsohn, E. Oñate, E. Dvorkin (Eds.), *In* Proceedings of the 4th World Congress on Computational Mechanics: New Trends and Applications, CIMNE, Barcelona, Spain, 1998, pp. 1–20.

[63] B. Hübner, E. Walhorn, D. Dinkier, Strongly coupled analysis of fluid-structure interaction using space-time finite elements, in: *In* Proceedings of the 2nd European Conference on Computational Mechanics, Cracow, Poland, 2001, pp. 546–547.

[64] H. G. Matthies, J. Steindorf, Partitioned strong coupling algorithms for fluid-structure interaction, Computers & Structures 81 (8) (2003) 805–812.

[65] P. R. F. Teixeira, A. M. Awruch, Numerical simulation of fluid-structure interaction using the finite element method, Computers & Fluids 34 (2) (2005) 249–273.

[66] K. M. Liew, W. Q. Wang, L. X. Zhang, X. Q. He, A computational approach for predicting the hydroelasticity of flexible structures based on the pressure Poisson equation, International Journal for Numerical Methods in Engineering 72 (13) (2007) 1560–1583.

[67] T. Yamada, S. Yoshimura, Line search partitioned approach for fluid-structure interaction analysis of flapping wing, CMES: Computer Modeling in Engineering & Sciences 24 (1) (2008) 51–60.

[68] C. Wood, A. J. Gil, O. Hassan, J. Bonet, A partitioned coupling approach for dynamic fluid-structure interaction with applications to biological membranes, International Journal for Numerical Methods in Fluids 57 (5) (2008) 555–581.

[69] Y. Bazilevs, V. M. Calo, T. J. R. Hughes, Y. Zhang, Isogeometric fluid-structure interaction: theory, algorithms, and computations, Computational Mechanics 43 (1) (2008) 3–37.

[70] A. L. Braun, A. M. Awruch, A partitioned model for fluid-structure interaction problems using hexahedral finite elements with one-point quadrature, International Journal for Numerical Methods in Engineering 79 (5) (2009) 505–549.

[71] M. Olivier, G. Dumas, J. Morissette, A fluid-structure interaction solver for nano-air-vehicle flapping wings, in: *In* Proceedings of the 19th AIAA Computational Fluid Dynamics Conference, American Institute of Aeronautics and Astronautics, San Antonio, Texas, USA, 2009, pp. 1–15.

[72] C. Habchi, S. Russeil, D. Bougeard, J.-L. Harion, T. Lemenand, A. Ghanem, D. D. Valle, H. Peerhossaini, Partitioned solver for strongly coupled fluid-structure interaction, Computers & Fluids 71 (2013) 306–319.

[73] J. Baiges, R. Codina, The fixed-mesh ALE approach applied to solid mechanics and fluid-structure interaction problems, International Journal for Numerical Methods in Engineering 81 (12) (2010) 1529–1557.

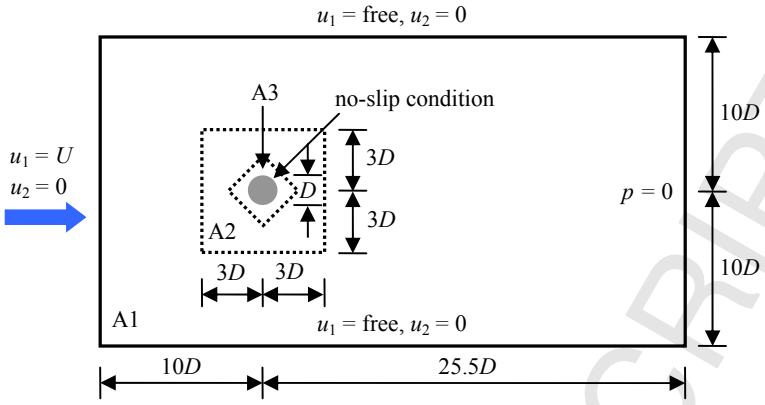

Fig. 1. Sketch of geometry and boundary conditions for the freely oscillating circular cylinder

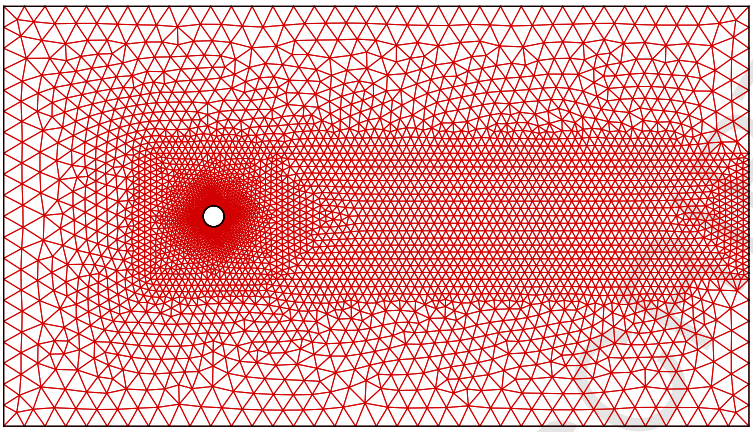

(a) Finite element mesh for the fluid field

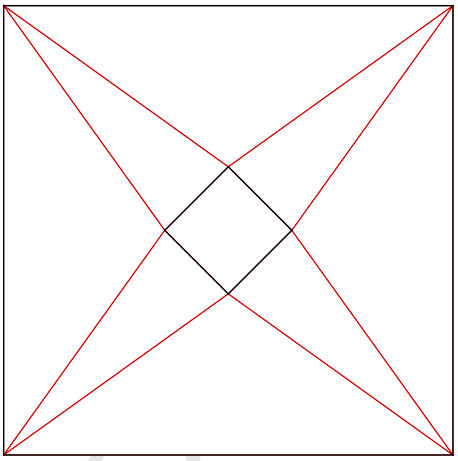

(b) MSA submesh for the ALE domain

Fig. 2. Mesh and submesh for the freely oscillating circular cylinder

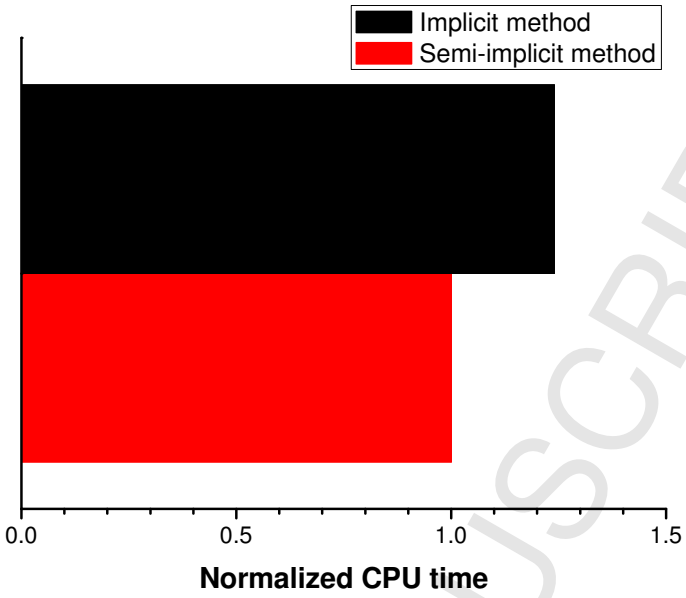

Fig. 3. Time cost of both methods for the oscillating circular cylinder

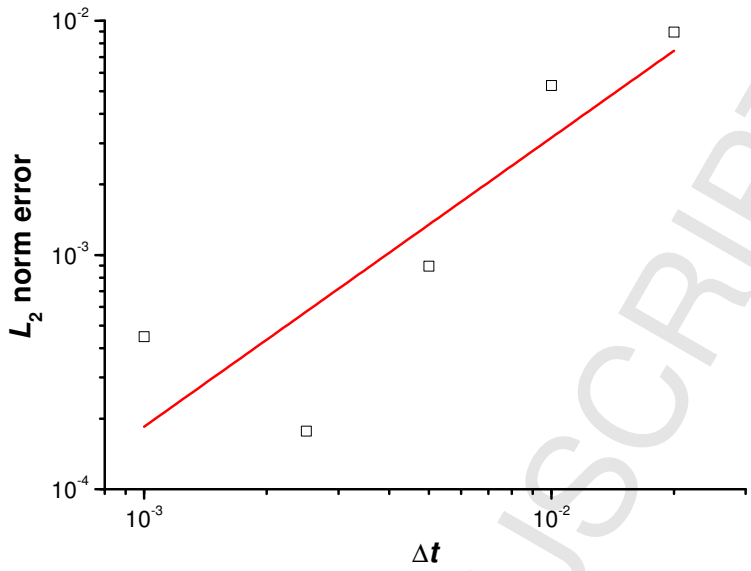

Fig. 4. Convergence study of the amplitude for the oscillating circular cylinder

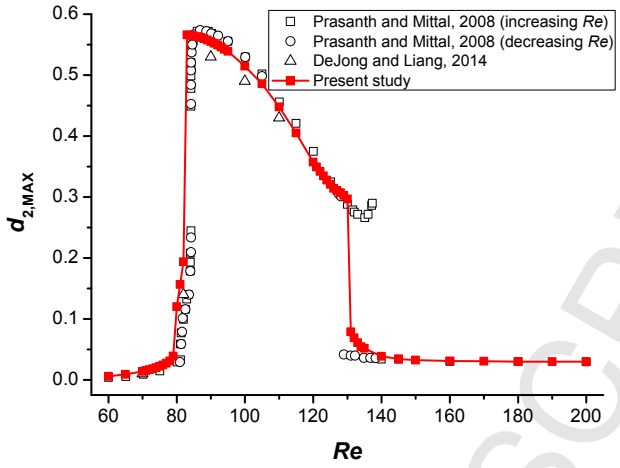

(a) Peak of vertical amplitude

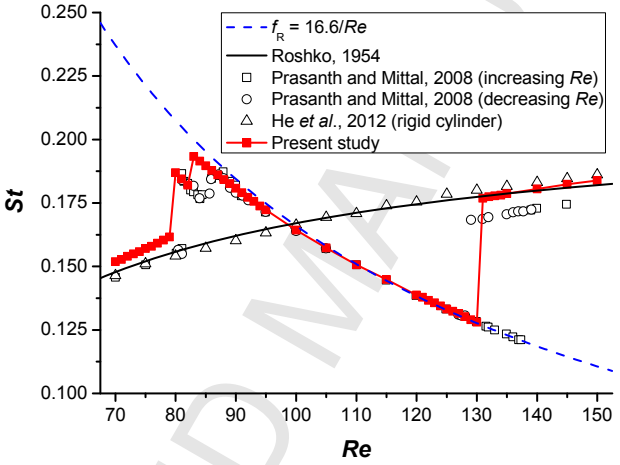

(b) Vortex-shedding frequency

Fig. 5. Variation of the cylinder response and the vortex-shedding frequency with Re

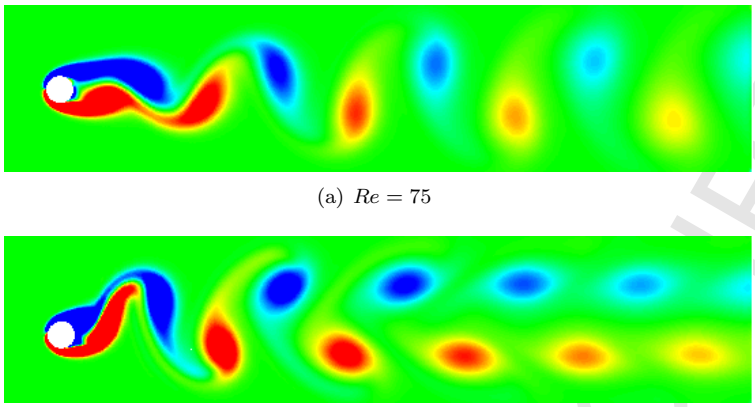

(a) $Re = 75$

(b) $Re = 90$

Fig. 6. Vorticity fields of the freely oscillating circular cylinder at two Re

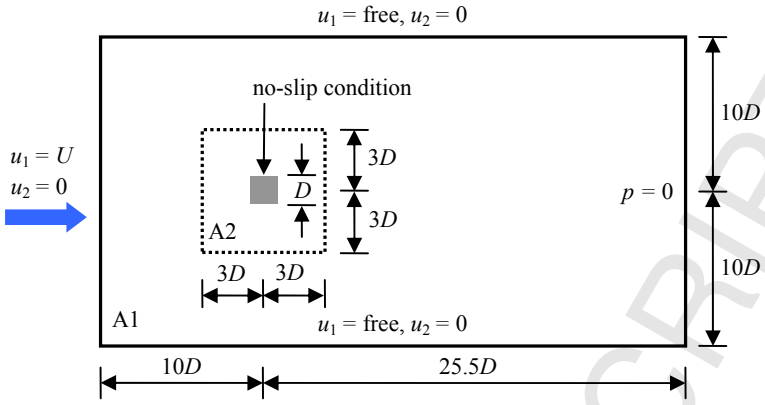

Fig. 7. Sketch of geometry and boundary conditions for the freely oscillating square cylinder

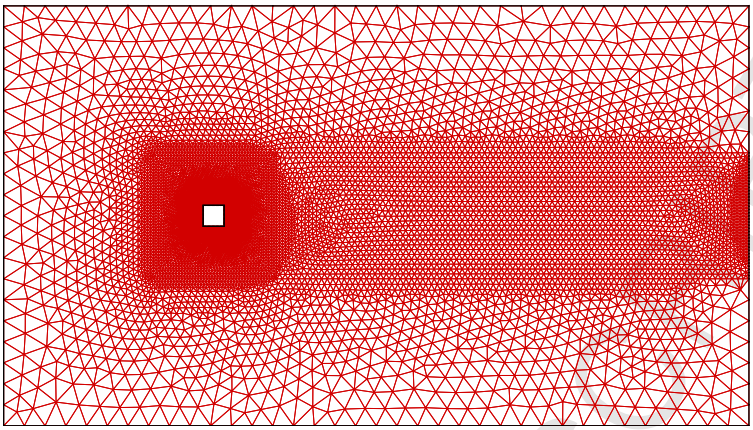

(a) Finite element mesh for the fluid field

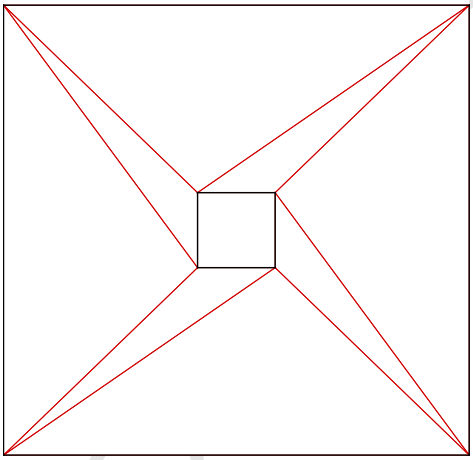

(b) MSA submesh for the ALE domain

Fig. 8. Mesh and submesh for the freely oscillating square cylinder

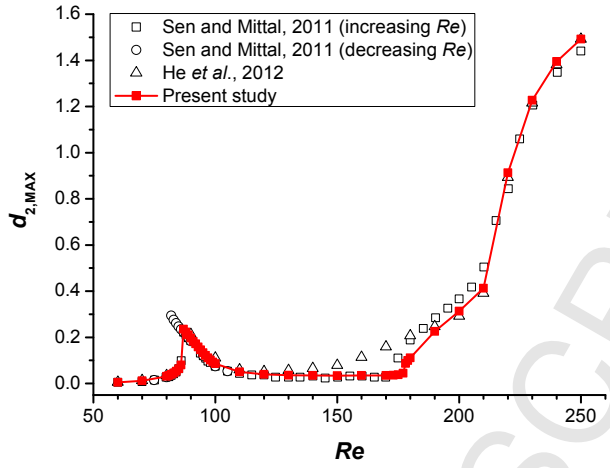

(a) Peak of vertical amplitude

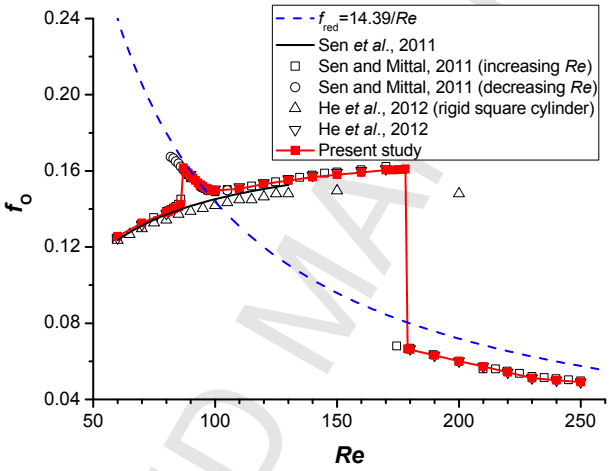

(b) Vortex-shedding frequency

Fig. 9. Variation of the cylinder response and the vortex-shedding frequency with Re

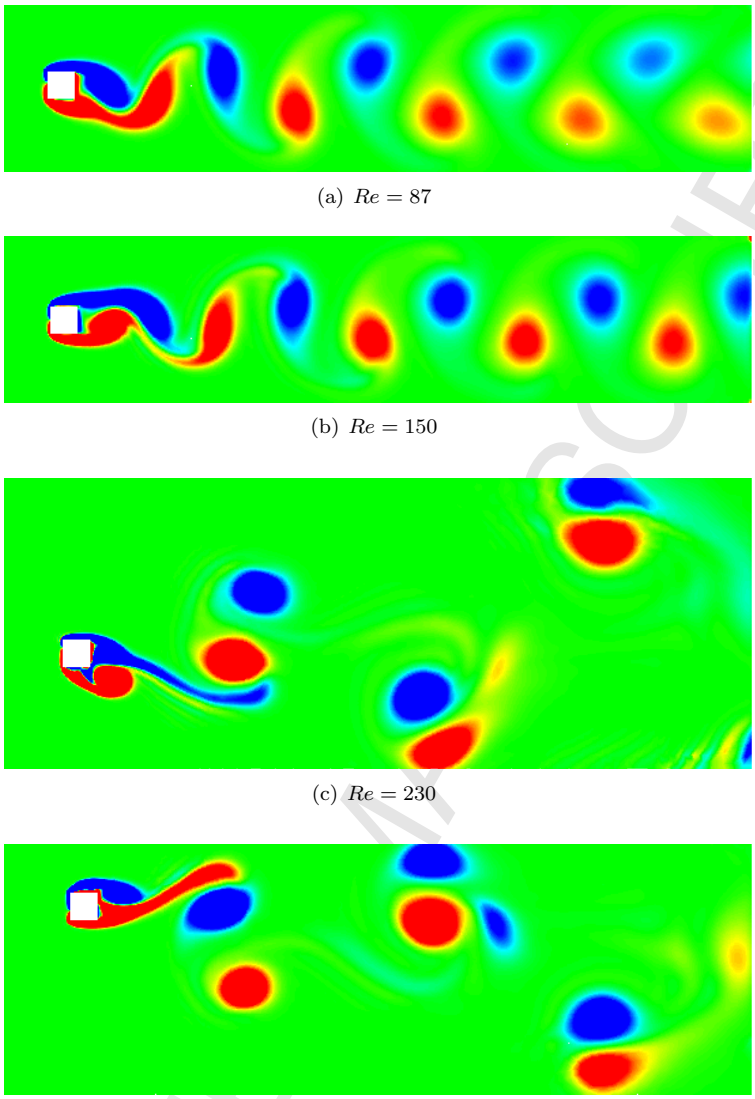

(a) $Re = 87$

(b) $Re = 150$

(c) $Re = 230$

(d) $Re = 250$

Fig. 10. Vorticity fields of the freely oscillating square cylinder at different Re

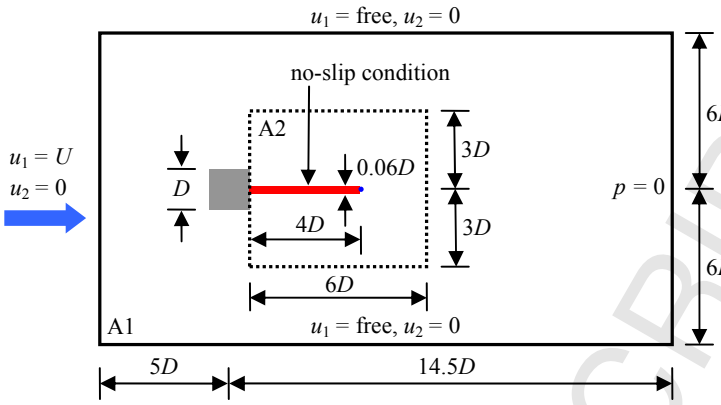

Fig. 11. Sketch of geometry and boundary conditions for the cantilever attached to a square cylinder

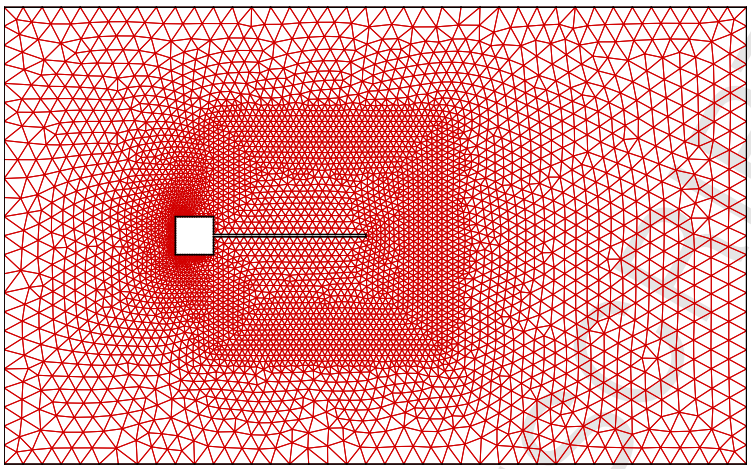

(a) Finite element mesh for the fluid field

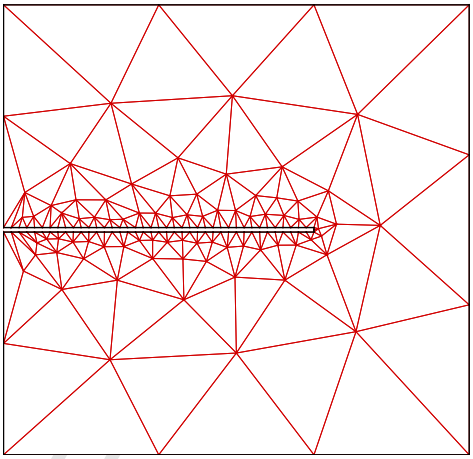

(b) MSA submesh for the ALE domain

Fig. 12. Mesh and submesh for Case 1

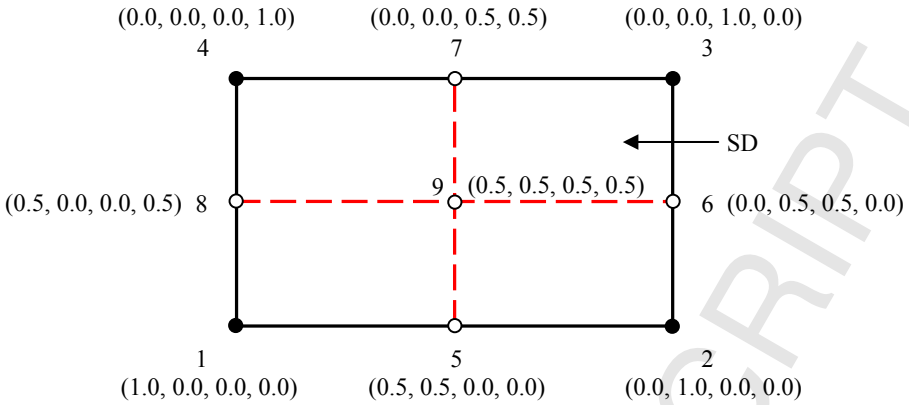

Fig. 13. Construction of SDs and smoothed shape functions in a Q4 element

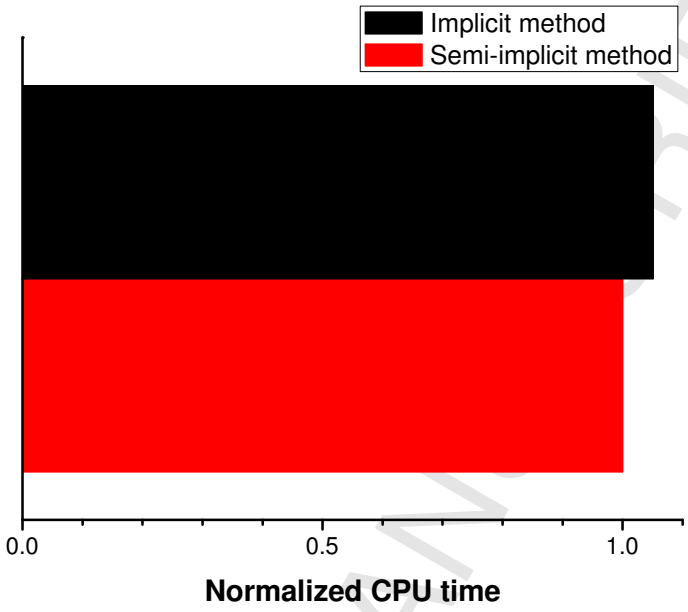

(a) $tol = 1.0 \times 10^{-6}$

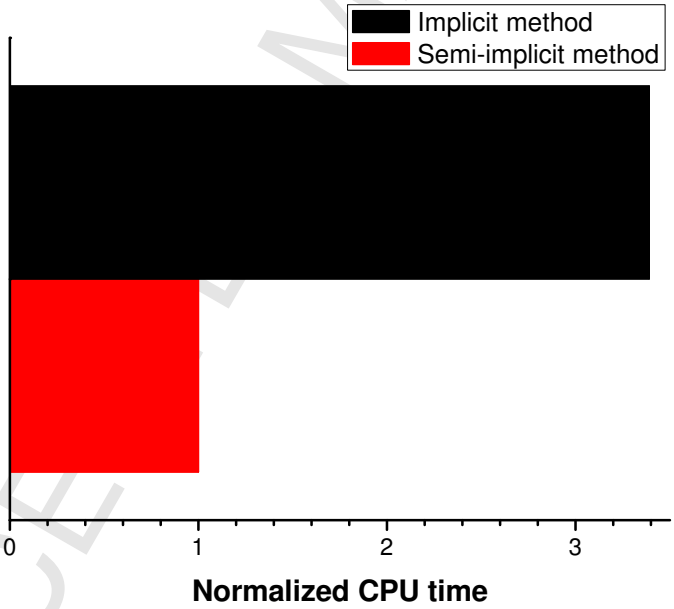

(b) $tol = 1.0 \times 10^{-7}$

Fig. 14. Time cost of both methods for the flexible cantilever

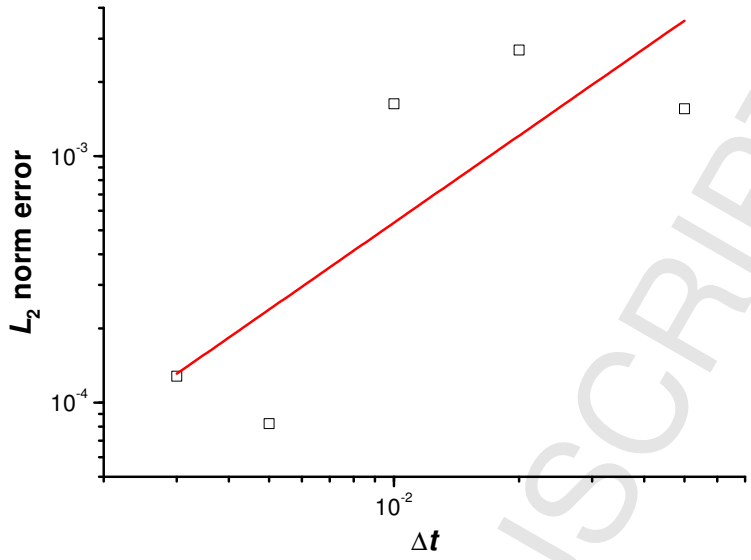

Fig. 15. Convergence study of the tip deflection for the flexible cantilever

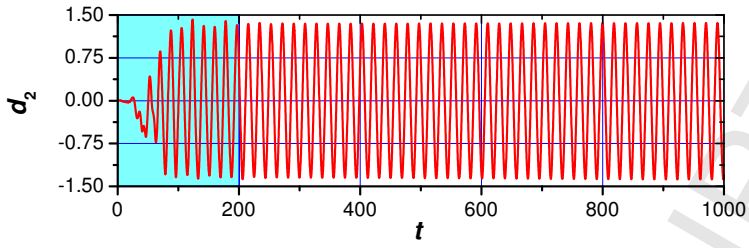

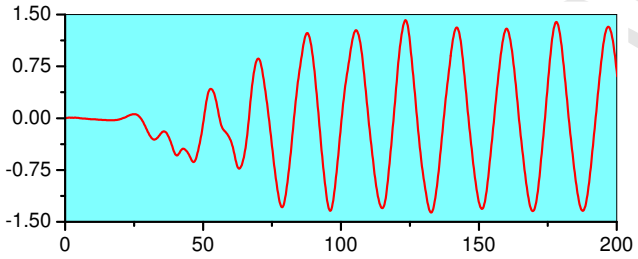

(a) Case 1

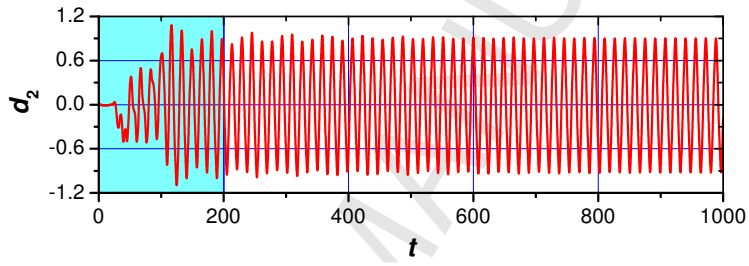

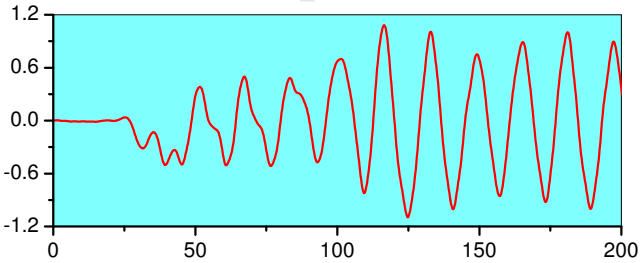

(b) Case 2

Fig. 16. Time history of vertical displacement of the measuring point

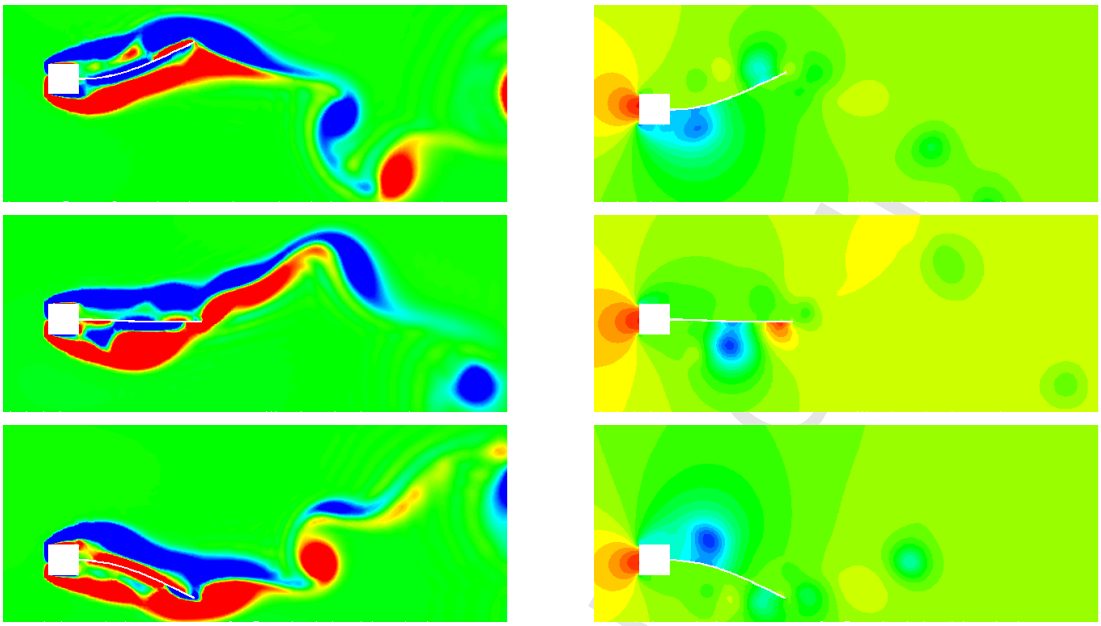

(a) Vorticity (b) Pressure

Fig. 17. Instantaneous contours of the flexible cantilever

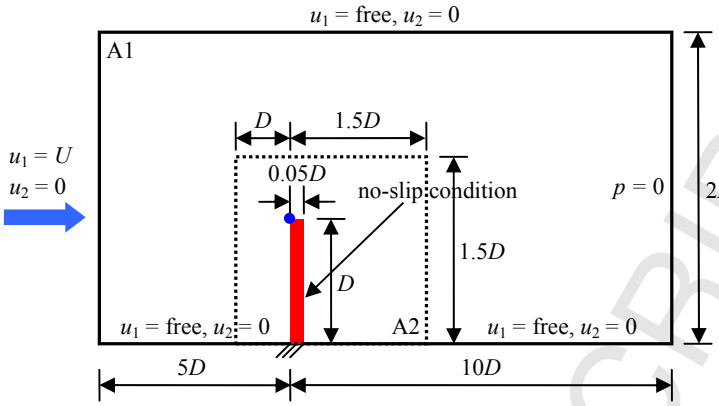

Fig. 18. Sketch of geometry and boundary conditions for the restrictor flap in a channel

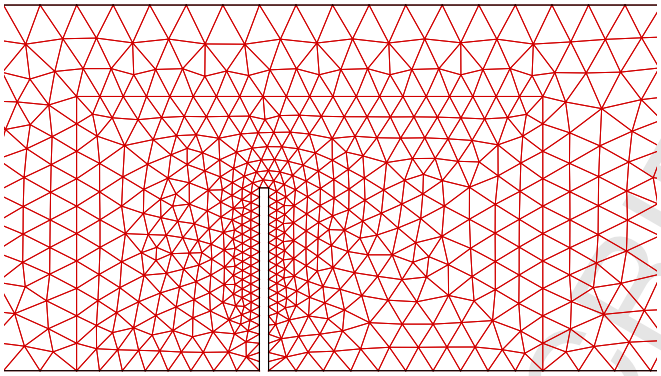

(a) Finite element mesh for the fluid field

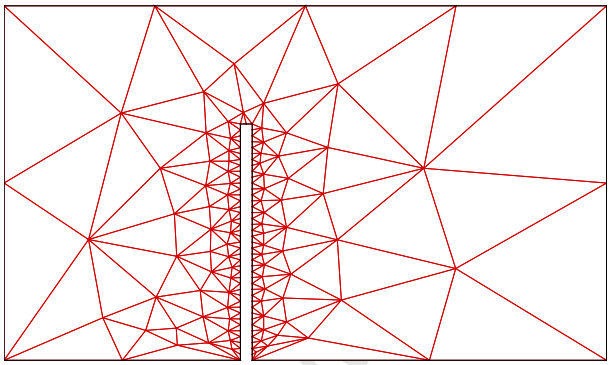

(b) MSA submesh for the ALE domain

Fig. 19. Mesh and submesh for Case 1

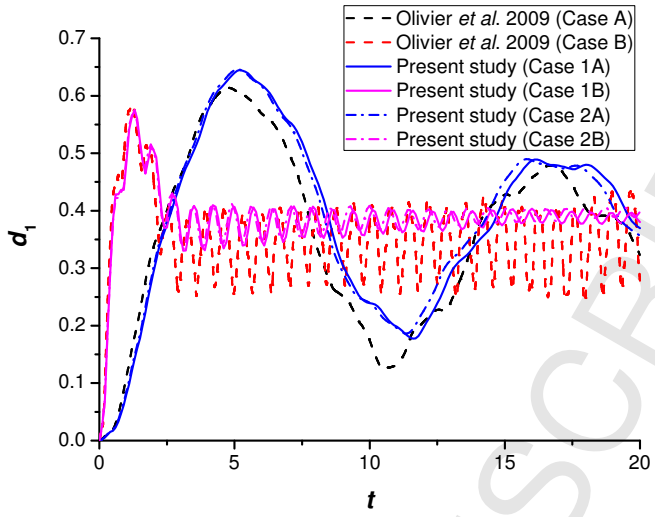

Fig. 20. Time history of horizontal displacement of the measuring point

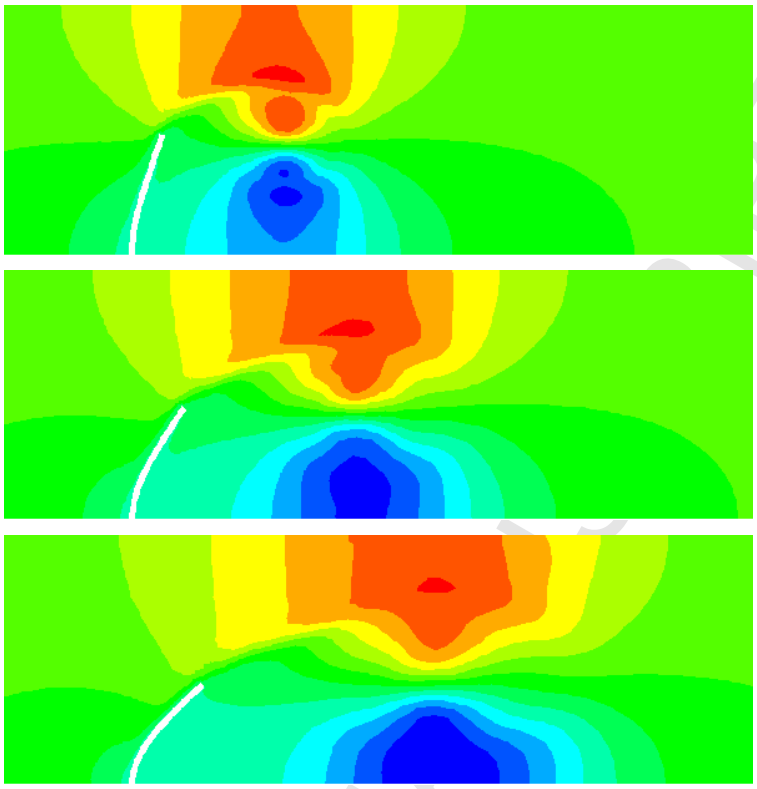

Fig. 21. Horizontal velocity contours of the flexible flap for Case A

Table 1. Comparison of results for the freely oscillating circular cylinder at $Re = 100$

Reference		$d_{1,\mathrm{MEAN}}$	$d_{1,\mathrm{RMS}}$	$d_{2,\mathrm{MAX}}$	$C_{\mathrm{D,MEAN}}$	$C_{\mathrm{D,RMS}}$	$C_{\mathrm{L,MAX}}$	St
Prasanth and Mittal [52] (M7k)		0.1115	0.00494	0.516	1.90	0.2486	0.1929	0.1643
Prasanth and Mittal [52] (M15k)		0.1100	0.00484	0.503	1.88	0.2434	0.1900	0.1644
He *et al.* [26]		0.1082	0.00465	0.515	1.81	0.2244	0.1985	0.1652
He *et al.* [15] (implicit)		0.1075	0.00477	0.515	1.84	0.2388	0.1887	0.1644
He *et al.* [15] (semi-implicit)		0.1075	0.00477	0.515	1.84	0.2388	0.1869	0.1644
Present study (M1)	tol_1	0.1075	0.00477	0.515	1.84	0.2388	0.1872	0.1644
	tol_2	0.1075	0.00477	0.515	1.84	0.2387	0.1870	0.1644
	tol_3	0.1075	0.00477	0.515	1.84	0.2388	0.1870	0.1641
Present study (M2)	tol_1	0.1068	0.00475	0.507	1.83	0.2349	0.1894	0.1641
	tol_2	0.1068	0.00475	0.507	1.83	0.2349	0.1898	0.1644
	tol_3	0.1068	0.00474	0.507	1.83	0.2347	0.1894	0.1641
Present study (M3)	tol_1	0.1059	0.00466	0.507	1.82	0.2343	0.2048	0.1647
	tol_2	0.1059	0.00466	0.507	1.82	0.2345	0.2069	0.1660
	tol_3	0.1059	0.00466	0.507	1.82	0.2343	0.2049	0.1647

Table 2. Comparison of results for the freely oscillating square cylinder at $Re = 90$

Reference	$d_{1,\mathrm{MAX}}$	$d_{1,\mathrm{RMS}}$	$d_{2,\mathrm{MAX}}$	$d_{2,\mathrm{RMS}}$	$C_{\mathrm{D,MEAN}}$	$C_{\mathrm{D,RMS}}$	$C_{\mathrm{L,MAX}}$	St
Sen and Mittal [58] (M1)	0.0907	0.0014	0.1843	0.1303	1.7917	0.0790	0.1082	0.1566
Sen and Mittal [58] (M2)	0.0906	0.0014	0.1822	0.1288	1.7882	0.0779	0.1026	0.1568
He *et al.* [26]	0.0959	0.0016	0.1998	0.1411	1.8831	0.0953	0.0687	0.1580
He *et al.* [15] (implicit)	0.0946	0.0016	0.1970	0.1391	1.8651	0.0905	0.0822	0.1574
He *et al.* [15] (semi-implicit)	0.0946	0.0016	0.1970	0.1391	1.8650	0.0905	0.0824	0.1574
Present study	0.0946	0.0016	0.1971	0.1391	1.8650	0.0905	0.0824	0.1574

Table 3. Information on the mesh and submesh generation

Subsystem	Meshing item	Case 1	Case 2
Fluid	Element type	T3	T3
	Number of elements	8789	13962
	Number of points	4508	7155
Solid	Element type	Q9	Q4
	Number of elements	20×1	80×2
	Number of points	123	243
MSA	Element type	T3	T3
	Number of elements	245	481
	Number of points	171	329

Table 4. Comparison of the present and previous results

Reference	Dimension	Coupling scheme	$d_{2,\mathrm{MEAN}}$	$f_{\mathrm{O,MEAN}}$
Wall and Ramm [62]	Two	Explicit	1.20	0.0604
Hübner *et al.* [63]	Two	Monolithic	1.08	0.0615
Matthies and Steindorf [64]	Two	Implicit	1.18	0.0610
Teixeira and Awruch [65]	Three	Explicit	1.35	0.0584
Dettmer and Perić [5]	Two	Implicit	1.25	0.0634
Liew *et al.* [66]	Two	Monolithic	1.34	0.0609
Yamada and Yoshimura [67]	Two	Implicit	1.19	0.0624
Wood *et al.* [68]	Three	Implicit	1.15	0.0573
Bazilevs *et al.* [69]	Two	Monolithic	1.21	0.0591
Braun and Awruch [70]	Three	Explicit	$1.181 \sim 1.215$	0.0591
Olivier *et al.* [71]	Two	Implicit	0.95	0.0618
Habchi *et al.* [72]	Two	Implicit	1.02	0.0634
Present study (Case 1)	Two	Implicit	1.24	0.0586
Present study (Case 1)	Two	Semi-implicit	1.25	0.0586
Present study (Case 2)	Two	Semi-implicit	0.92	0.0622

Table 5. Information on the mesh and submesh generation

Subsystem	Meshing item	Case 1	Case 2
Fluid	Element type	T3	T3
	Number of elements	2301	2786
	Number of points	1260	1523
Solid	Element type	Q8	Q4
	Number of elements	20×1	40×2
	Number of points	103	123
MSA	Element type	T3	T3
	Number of elements	258	258
	Number of points	177	177

1. Interface coupling conditions are achieved via the MCIBC method.
2. The MCIBC method is weakly implemented based on the full fluid stress tensor.
3. A CBS-based partitioned semi-implicit coupling algorithm is proposed.
4. The semi-implicit algorithm works for FSI in conjunction with the MCIBC method.